Three Days-Ahead Solar Irradiance Forecasting in Burkina Faso: A Comparison of WRF-Solar Model and Machine Learning Approaches

UNIVERSITE JOSEPH KI-ZERBO

ECOLE DOCTORALE INFORMATIQUE ET CHANGEMENT CLIMATIQUE (EDICC)

BURKINA FASO

La Patrie ou la Mort, nous Vaincrons

Order N° : .....

MASTER RESEARCH PROGRAM

SPECIALITY: INFORMATICS FOR CLIMATE CHANGE (ICC)

MASTER THESIS

subject

Three Days-Ahead Solar Irradiance Forecasting in Burkina Faso: A Comparison of WRF-Solar Model and Machine Learning Approaches.

Presented 09/07/2025, by:
GNOULA Aimé

Examination Jury

Members:

Pr Sié KAM	Professeur titulaire, Transferts Thermique, Energétique, UFR-SEA, UJKZ, Burkina Faso	**President**
Dr Alain DIASSO	Maitre-assistant, Département Energie Institut du Génie de l'Environnement et du Développement Durable	**External Examiner**
Dr Sié Zacharie KAM	Maître de Conférence Physique, UFR-SEA, Université Joseph KI-ZERBO	**Major Supervisor**
Dr Windmanagda SAWADOGO	Institute of Meteorology and Climate Research (IMK-IFU), Karlsruhe Institute of Technology (KIT)	**Co-Supervisor**

WASCAL 2024-2025

Dedication

I dedicate this thesis to:

My beloved mother, and my dear father.

Acknowledgements

Foremost, I would like to express my sincere gratitude to the funders the Federal Ministry of Education and Research (BMBF) and WASCAL (West African Science Service Centre on Climate Change and Adapted Land Use) for fully supporting my master's studies.

I extend my heartfelt thanks to the Director of the "École Doctorale Informatics for Climate Change" (ED-ICC), Prof. Amadé OUEDRAOGO, and the Deputy Director, Dr Ousmane COULIBALY, for their continuous engagement and guidance throughout the program. My appreciation also goes to our Scientific Coordinator, Dr Benewindé Jean-Bosco ZOUNGRANA, and the entire ED-ICC staff for their unwavering support.

I am grateful to the jury members who will evaluate the quality of this thesis. I also thank the Director of the WASCAL Competence Center (CoC), Prof. Kehinde O. Ogunjobi, for granting me the opportunity to be part of this prestigious research institution an inspiring environment that brings together researchers committed to climate change adaptation and mitigation.

I am deeply indebted to my dedicated supervisors, Dr Sié Zacharie KAM and Dr Windmanagda SAWADOGO, for their mentorship, guidance, encouragement, and invaluable insights throughout this research journey. I am honoured to have learned from you and your brilliant assistants.

Special thanks also go to the scientists of the WASCAL Competence Center, including Dr. Seyni SALACK, for generously sharing his scientific expertise, and Dr Abdoul Aziz Diallo BELKO and Dr Kwame Oppong HACKMAN who provided me valuable tools.

At the same time, my thanks go to members of jury such as Pr Sié KAM and Dr Alain DIASSO.

I extend my warmest appreciation to my beloved parents, my constant counsellors, and to my entire family, especially my siblings, for their love, encouragement, and unwavering support.

My gratitude also goes to the members of "WASCAL MRP-ICC Batch 1, 2 and 3" for their guidance as elders, and to my wonderful colleagues from "WASCAL MRP-ICC Batch 4" for their friendship, teamwork, and cooperation throughout this journey.

Finally, from the bottom of my heart, I thank all individuals who contributed, directly or indirectly, to the realization of this work.

Abstract

The increasing production on solar photovoltaic (PV) energy in Burkina Faso necessitates accurate forecasting of solar irradiance to optimize grid production and power planning. This study evaluates and compares the performance of the physics-based WRF-Solar model and three machine learning (ML) techniques such as Random Forest (RF), Support Vector Regression (SVR), and Long Short-Term Memory (LSTM) for three-day-ahead forecasting of Global Horizontal Irradiance (GHI). Using ground-based measurements from the Zagtouli solar farm and reanalysis data from ERA5, CAMS, and ECMWF-HRES for the year 2020, the research analyses model performance under diverse atmospheric conditions, including clear-sky, cloudy, high aerosol, and mixed (cloudy + aerosol) scenarios. The methodology includes quality control of observations, sky condition classification using the clearness index, and model evaluation using statistical metrics such as RMSE, MAE, R^2, and IOA. Results demonstrate that WRF-Solar outperforms 3 ML models used in this thesis under clear sky condition. Under cloudy condition, ML models particularly LSTM has given better prediction compared to WRF-Solar models. No clear winner between models under aerosol condition, while in mixed condition, the WRF-solar and LSTM have shown a continue competency for the three days ahead solar irradiance forecasting.

The study concludes that ML methods offer a promising alternative or complement to traditional physical models in solar forecasting in West Africa's dynamic climate.

Keywords: Global Horizontal Irradiance; WRF-Solar; Machine Learning; Burkina Faso; Days-ahead forecasting, Climate**.**

Resumé

La production continue de l'énergie solaire photovoltaïque (PV) au Burkina Faso nécessite une prévision précise de l'irradiance solaire afin d'optimiser la production du réseau et la planification énergétique. Cette étude compare les performances du modèle WRF-Solar basé sur la physique et de trois techniques d'apprentissage automatique (IA) telles que la forêt aléatoire (RF), la régression à vecteurs de support (SVR) et la mémoire à long terme (LSTM) pour la prévision à trois jours de l'irradiance horizontale globale (GHI). À l'aide de mesures au sol du parc solaire de Zagtouli et de données de réanalyse d'ERA5, CAMS et ECMWF-HRES pour l'année 2020, la recherche analyse les performances du modèle dans diverses conditions atmosphériques, notamment des scénarios de ciel clair, nuageux, à forte concentration d'aérosols et mixtes (nuageux + aérosols). La méthodologie comprend le contrôle qualité des observations, la classification des conditions du ciel à l'aide de l'indice de clarté et l'évaluation du modèle à l'aide de mesures statistiques telles que RMSE, MAE, R^2 et IOA. Les résultats démontrent que WRF-Solar surpasse les trois modèles ML utilisés dans cette thèse pour ciel clair. Aux temps nuageux, les modèles ML, et notamment le LSTM, ont donné de meilleures prévisions que le modèle WRF-Solar. Au temps à forte concentration d'aérosols, aucun ne fait mieux par rapport au modèle de persistance. Par contre, à la condition mixte, le modèle WRF-Solar et le LSTM montrent une concurrence continue sur les trois jours de prédiction. L'étude conclut que les méthodes ML offrent une alternative prometteuse, voire un complément, aux modèles physiques traditionnels pour la prévision solaire dans le contexte climatique dynamique de l'Afrique de l'Ouest.

Mots clés : Irradiation Horizontale Globale ; WRF-Solar ; Apprentissage automatique ; Burkina Faso ; Trois jours d'avance de prévision, Climat**.**

Acronyms and abbreviations

AOD_{550}	**:**	Total Aerosol Optical Depth at 550 nm
AWS	**:**	Automatic Weather Station
BSRN	**:**	Baseline Surface Radiation Network
CAMS	**:**	Copernicus Atmosphere Monitoring Service
ECMWF-HRES	**:**	European Centre for Medium-Range Weather Forecasts highest-resolution
ERA5	**:**	Fifth generation ECMWF Atmospheric Reanalysis
GHI	**:**	Global Horizontal Irradiance
ICC	**:**	Informatics for Climate Change
ILBC	**:**	Initial and Lateral Boundary Conditions
IOA	**:**	Index of Agreement
LSTM	**:**	Long Short-Term Memory
MAE	**:**	Mean Absolute Error
ML	**:**	Machine Learning
nMAE	**:**	normalised Mean Absolute Error
nRMSE	**:**	normalised Root Mean Square Error
NWP	**:**	Numerical Weather Prediction
PBL	**:**	Planetary Boundary Layer
PV	**:**	Photovoltaic
R^2		Coefficient of determination
RF	**:**	Random Forest
RMSE	**:**	Root Mean Square Error
RRTMG	**:**	updated Rapid Radiative Transfer
s	**:**	Skill score
SVR	**:**	Support Vector Regression
WASCAL	:	West African Science Service Centre on Climate Change and Adapted Land Use
WRF-Solar	**:**	Weather Research and Forecasting with extension Solar

Nomenclature

IOA	**:**	**Dimensionless**
MAE	**:**	**W/m^2**
nMAE	**:**	**W/m^2**
nRMSE	**:**	**W/m^2**
R^2	**:**	**Dimensionless**
RMSE	**:**	**W/m^2**
s	**:**	**Dimensionless**

List of Tables

List of Figures

Introduction

The growing global demand for clean and renewable energy has made solar power a key component of sustainable energy strategies (Maka & Alabid, 2022). Among the renewable technologies, solar photovoltaic (PV) systems have gained widespread attention due to their potential to reduce greenhouse gas (GHG) emissions and expand electricity access in off-grid, grid-connected, and rural areas (Allal et al., 2024).

This is especially relevant in Burkina Faso, where electrification remains limited in many regions and solar energy presents a promising path to address energy access challenges.

As the energy sector accounts for nearly 40% of global GHG emissions (Wang et al., 2018), the adoption of solar PV is also critical in addressing climate change. The Paris Agreement underscores the urgency of reducing emissions to limit global temperature rise below 2°C by the end of the century (Nawab et al., 2023).

In this context, solar PV systems not only provide a clean and sustainable power source but also play a vital role in climate mitigation efforts (F. Wang et al., 2018; Nawab et al., 2023).

However, the effective integration of solar power into the energy grid depends heavily on accurate forecasting of solar irradiance, the rate at which solar energy reaches the Earth's surface. Solar irradiance forecasting enables better planning of energy production, improves grid stability, and reduces uncertainty in power supply (N. Zhou et al., 2024).

This is particularly important in countries like Burkina Faso, where solar potential is high (Azoumah et al., 2010) but can be affected by seasonal and meteorological variability.

Forecasting methods range from physical models such as the Weather Research and Forecasting (WRF) model to advanced Machine Learning (ML) techniques. The WRF-Solar model, an extension of the WRF framework, is specifically designed to improve solar irradiance forecasts by incorporating atmospheric physics, cloud dynamics, and radiative transfer processes (Perez et al., 2013; de Lima et al., 2025).

While WRF-Solar has been successfully applied in various regions (Eissa et al., 2018; Diagne et al., 2014; Lara-Fanego et al., 2012), its performance can be constrained by model complexity, parameterization choices, and input data uncertainty.

1. Statement of the problem

Burkina Faso is one of the sunniest countries in West Africa and is facing the challenges posed by Climate Change in the Sahel region (Abid et al., 2021).

Climate Change, with its increase in rainfall patterns, on temperature, will negatively affect socioeconomic sectors in Burkina Faso such as agriculture (Sawadogo et al., 2024). In Burkina Faso, the agriculture sector accounts for 90% of the labour force. This is the primary occupation of the rural population and contributes up to 38% of GDP (Crawford et al., 2016).

In 2023, Burkina Faso reported that about 52.20% of its national population had access to electricity, with only 7.02% in rural areas compared to 87.04% in urban areas (DGESS, 2023). Recognizing this disparity, the government has set a target to raise the national electrification rate to 65% by 2030, aiming for 95% coverage in urban areas and 50% in rural areas (Abid et al., 2021). Achieving this ambitious goal highlights the critical need for research on accurate energy forecasting, which can support the development of sustainable and equitable energy access across both urban and rural regions.

However, the efficiency and reliability of solar energy systems heavily depend on accurate solar radiation forecasting. Traditional methods, such as dynamical downscaling models, offer valuable insights but are limited by computational demands and potential inaccuracies in certain conditions (Sawadogo et al., 2024). Machine Learning (ML) models are emerging as powerful tools for solar prediction but require robust data and validation (Fraihat et al., 2022).

The comparative performance of dynamical downscaling models and ML models in the specific context of Burkina Faso's climatic conditions remains underexplored. Questioning this gap could enhance the deployment and management of solar energy systems, finally contributing to the country’s energy security and climate goals either in rural or urban areas.

In regions like Burkina Faso, where solar energy holds immense potential due to consistently high solar irradiance levels, the need for accurate short- to mid-term solar forecasts is critical for effective grid management and energy planning. However, forecasting remains challenging due to atmospheric variability, limited meteorological infrastructure, and the performance limitations of traditional physical and statistical models. The Weather Research and Forecasting model with solar extensions (WRF-Solar) is a popular physics-based tool, but ML models offer alternative data-driven methods that may outperform WRF under certain conditions. This research investigates the problem of three-day-ahead solar irradiance forecasting in Burkina Faso by comparing the performance of WRF-Solar and ML models. It seeks to determine which method provides more reliable, accurate, and contextually adaptable forecasts for the West African region's unique climatological patterns and infrastructural constraints.

2. Research Questions

2.1. Main research

Accurate solar irradiance forecasting is essential for optimizing solar energy production and grid integration, especially in regions like Burkina Faso, where solar power is so important and plays a crucial role in energy sustainability and security. This study aims to evaluate and compare the performance of the WRF-Solar model and ML approaches for days-ahead solar irradiance forecasting under different atmospheric conditions. To guide this investigation, the main research question is as follows:

Can ML methods outperform WRF-Solar model on days-ahead solar irradiance forecasting?

2.2. Specific questions

To carry out this study, three specific questions arise:

1. How does the forecasting accuracy of ML models compare to that of WRF-Solar under clear-sky conditions?
2. In cloudy conditions, how do ML models perform relative to the WRF-Solar model in predicting solar irradiance?
3. To what extent do ML models outperform WRF-Solar in forecasting solar irradiance during high aerosol conditions?
4. How do ML and WRF-Solar models compare in accuracy under combined cloudy and high aerosol conditions?

3. Hypotheses

3.1. The main hypothesis

The main hypothesis of this research is ML models outperform the WRF-Solar model in days-ahead solar irradiance forecasting.

3.2. Specific hypotheses

Regarding the main hypothesis, three hypotheses were put forward in the context of this study:

1. Under clear-sky conditions, ML models achieve forecasting accuracy that matches or exceeds that of WRF-Solar.
2. In cloudy conditions, ML approaches exhibit good performance than the WRF-Solar model.
3. When aerosol levels are high, ML models demonstrate forecasting capabilities that rival or surpass WRF-Solar.

4. For mixed cloudy and aerosol conditions, ML techniques deliver equal or improved prediction accuracy compared to WRF-Solar.

4. Objectives

4.1. General Objective

The main objective of this study is to evaluate the performance of ML methods against the WRF-Solar model for days-ahead solar irradiance forecasting.

4.2. Specific Objectives

This main objective is divided into three specific objectives:

1. To compare the forecasting accuracy of ML models and the WRF-Solar model under clear-sky conditions;
2. To assess the WRF-Solar and ML techniques under cloudy conditions;
3. To evaluate the WRF-Solar and ML predictive accuracy in the presence of high aerosol concentrations;
4. To examine their forecasting capabilities under combined cloudy and aerosol-laden atmospheric conditions.

5. Aim of the study

The aim of leading three days-ahead solar irradiance forecasting in Burkina Faso involves comparing the Weather Research and Forecasting (WRF-Solar) Solar model with three most popular ML approaches used in Global Horizontal Irradiance (GHI) forecasting to determine which method provides more accurate and reliable predictions. This comparison is crucial for optimising solar energy integration into the power grid, ensuring stability, and reducing the uncertainty associated with solar power generation. The research focuses on evaluating the performance of these models in terms of accuracy, error reduction, and computational efficiency.

6. Plan of the thesis

The remainder of this thesis structured as follows:

Section 1 reviews existing literature on solar irradiance forecasting, discussing both numerical weather prediction and ML approaches. Section 2 presents the methodology, detailing the data sources, preprocessing steps, and modelling techniques used in the study. Section 3 provides

comparative analysis of forecast results, with key findings, highlighting the strengths and weaknesses of each approach, and recommendations for future research.

Chapter 1: Literature review

This literature review presents the main results of other researchers or authors in the domain of GHI forecasting related to our study by using Numerical Weather Predictions (NWP) or ML models. It covers Forecasting Techniques, ML in Solar Prediction, and African Studies.

1.1 Forecasting Techniques for Solar Irradiance

Forecasting solar irradiance is essential for the reliable planning and management of solar energy systems. Methods are broadly categorised into physical, statistical, and hybrid approaches (Solano et al., 2022; Odejobi et al., 2024).

Among the physical models, the Weather Research and Forecasting model with its Solar extension (WRF-Solar) is one of the most recognised Numerical Weather Prediction (NWP) models, designed to simulate atmospheric processes relevant to solar irradiance, such as radiation transfer, aerosols, and cloud dynamics (Jimenez et al., 2016; J. Yang et al., 2021; Virgianto, 2024).

Recent studies have shown that WRF-Solar provides accurate short- to medium-term forecasts when properly configured with localised datasets and aerosol parameterization. In Brazil, de Lima et al. (2025) compared WRF-Solar with GFS-MOS and concluded that WRF-Solar achieved significantly better temporal resolution and accuracy for medium-term (72-hour) forecasts. Similarly, in Ghana, Sawadogo et al. (2023a) demonstrated that WRF-Solar, when integrated with aerosol optical depth (AOD) data, showed substantial improvements in the prediction of GHI.

Jimenez et al. (2016) demonstrated WRF-Solar's ability to reduce irradiance errors by 20% under clear skies by incorporating aerosol feedback. Always in the ability of WRF-Solar to perform better, Yoon et al. (2025) demonstrated that WRF-Solar exhibits better performance compared to the WRF model in South Korea.

Despite these strengths, WRF-Solar poses challenges: it is computationally expensive, sensitive to physics scheme configurations, and highly dependent on the quality and availability of input data (Sawadogo, et al., 2024; Zhang et al., 2023; Y. Liu et al., 2022).

In fact, the quality of model outputs relies to a large extent on the availability and quality of input data sets, such as aerosol properties, surface albedo, and initial atmosphere parameters. Furthermore, the success of the model also relies on the selection of physics schemes (microphysics, radiation, and boundary layer) with the requirement of proper tuning to the local environment (X. Zhou et al., 2024). Poor or outdated land-use and topographic data can also

impact negatively on the model's performance, particularly over heterogeneous areas (Kirthiga & Patel, 2018).

In general, WRF-Solar has been discovered to be highly promising for the estimation of solar irradiance on short to medium time scales in different geographic environments, particularly when it is tuned with localized aerosol and atmospheric input data. Its use is constrained by computational expense, sensitivity to system configuration, and sensitivity to high-quality input data. To achieve the full capability of the model, the shortcomings must be surmounted, especially in resource-constrained and data-sparse areas such as sub-Saharan Africa.

1.2 Machine Learning in Solar Prediction

Machine learning (ML) techniques, such as Random Forest (RF), Support Vector Regression (SVR), K-Nearest Neighbors (KNN), and complex deep learning structures like Long Short-Term Memory (LSTM) and Artificial Neural Networks (ANNs), have become widely recognized in the field of solar irradiance and power prediction. The capacity of these methods to identify nonlinear interactions and time-varying changes without requiring large amounts of physical data inputs makes them especially useful in situations with limited data availability or resource constraints.

Many studies have shown the high efficiency of LSTM models, which can be applied to process time-series data. For example, Díaz-Bedoya et al., (2023) between Andean cities, that compared LSTM against autoregressive (AR) and RF models. Even if the RF and the LSTM provided the same accuracy (MAPE ≈ 25%) the LSTM was the best model in reducing RMSE and MAE by 10 W/m² approximately compared to AR. However, even powerful LSTM models need large datasets and may be sensitive to the data quality and hyperparameter selection.

Other studies have leveraged satellite data for ML-based forecasting. Li et al. (2023), working on Indian Ocean islands, used satellite-derived features in both LSTM and linear regression models for hourly GHI prediction. LSTM again proved robust, though the study noted that interpretability remains a challenge, and the need for large labelled datasets can limit transferability to regions with sparse historical data.

ANNs have also shown promise in capturing the complex relationship between meteorological inputs and solar output. For example, Winster Praveenraj et al. (2024) demonstrated the superiority of ANN models over traditional methods in Morocco, particularly under both clear and variable sky conditions. However, the study acknowledged the “black box” nature of ANN models, which limits transparency and trust in operational forecasting systems.

Hybrid models combining ML algorithms are increasingly used to boost performance. Saxena et al. (2024) developed a KNN-SVM hybrid model that achieved 98% accuracy in solar power forecasting in Jodhpur, India. The complementary strengths of KNN (local similarity) and SVM (generalisation power) proved effective, yet the method's sensitivity to outliers and feature scaling was noted as a limitation.

Ensemble methods such as Random Forest (RF) and Gradient Boosting (XGBoost) are commonly used because they are reliable and have simple training procedures. Murdan and Armoogum (2023) showed that RF gave best accuracy than other models in predicting hourly solar power generation in Germany. However, tree-based methods can have challenges in handling temporal dependencies and might require careful feature engineering to really capture the nature of the time series data.

In more recent studies, cutting-edge deep learning technologies have been explored. Naveed et al. (2025) proposed a stacked ensemble model of ANN, RF, and SVM and obtained an R^2 of 0.9979 on irradiance prediction. Although high accuracy was achieved by this architecture, its computational cost and model complexity fall beyond the reach of real-time applicability in low-resource settings. Camacho et al. (2025) introduced attention-augmented LSTMs that enhanced the model's ability to learn long-term dependencies. Similarly, physics-constrained LSTM models proposed by Winster Praveenraj et al. (2024) implemented physical laws, and accuracy grew if there was missing or noisy data. However, discovering the balance between the flexibility of the model and physical consistency remains an open research problem.

A summary of different techniques used in solar irradiance forecasting is described in the Table 1.

Table 1: summary of techniques used on solar irradiance forecasting

Feature	**Physical Models**	**Statistical Models**	**Machine Learning**
Based on	Physics equations	Historical patterns	Data-driven learning
Computational Cost	High	Low	High
Accuracy in Clear Weather	High	Moderate	High
Accuracy in Unstable Weather	Low	Moderate	High

Interpretability	Easy to understand	Easy to understand	Hard to interpret
Best For	Long-term forecasting	Short-term forecasting	Complex-forecasting problems

1.3 African Studies: Regional Gaps.

Africa has special environment for solar prediction with its high solar resources, sparse ground-based monitoring infrastructure, and complex atmospheric processes like pervasive dust storms, penetrating convective events, and changing aerosol loading. The conditions present a challenge and a window for the creation of prediction methods specific to the continent's needs. Yet, Africa remains vastly under-addressed within high-resolution solar prediction endeavours, especially where the performance under operation and real-world implementation conditions are accounted for.

Key studies in recent years have begun to address this gap:

In West Africa, Sawadogo et al. (2023b, 2024) evaluated the performance of WRF-Solar and reanalysis data against ground truth in Ghana and Burkina Faso, providing essential benchmarks for regional forecasting systems.

In Egypt, Khamees et al. (2024) tested three shortwave radiation schemes in WRF-Solar and found that model accuracy varied significantly with AOD input sources, highlighting the importance of aerosol data in North Africa.

In Morocco, Mendyl et al. (2024) compared ML models with traditional techniques and showed superior performance using ensemble techniques and local calibration.

A study in 2025 conducted in Nairobi assessed various WRF-Solar radiation schemes (RRTMG) and compared model outputs with ground-based irradiance measurements. It found notable differences in Mean Square Error across schemes, with RRTMG performing best overall (Mwigereri et al., 2025)

Moreover, Mabasa et al. (April 2025) evaluated the performance of the GFS model for global horizontal irradiance (GHI) across six climate zones in South Africa. Findings show satisfactory forecast skill, especially inland, with forecast reliability decreasing over time.

Then, Hayawi et al. (May 2025) carried out ML forecasting in dust-prone Morocco, benchmarking six algorithms (SVR, ANN, RF, XGBoost, etc.) for daily solar power prediction at a solar plant in Benguerir, highlighting the impacts of aerosol conditions.

Lastly, Zwane et al. (2022) conducted a bibliometric analysis of African solar forecasting (2000–2021), revealing rapid growth post-2015, with South Africa leading the output. Key themes include solar irradiance modelling, AI methods, and clear-sky analysis.

Despite these valuable contributions, a significant gap persists in the literature regarding the fact that none of study compare the operational performance of WRF-Solar and ML-based models' side by side under various weather conditions for lead times beyond 24 hours, a crucial horizon for energy planning and grid management.

Chapter 2: Materials and methodology

This section presents the study area, the data used for simulating the WRF-Solar, the ML models, and all the procedures we have applied to preprocess the raw data and create the final dataset.

2.1 Study area

This study focuses on the Zagtouli Solar Power Plant, the largest grid-connected solar photovoltaic (PV) facility in Burkina Faso. Located in Zagtouli, a village on the outskirts of Ouagadougou, the capital city, the plant occupies approximately 51 hectares and has an installed capacity of 33 megawatts (MW). Commissioned in 2017 with support from international partners, including the European Union and the French Development Agency, the plant plays a vital role in Burkina Faso's energy transition by supplying clean electricity to the national grid and reducing reliance on fossil fuel-based generation and electricity imports.

Zagtouli lies within the Sahelian climatic zone, characterized by high solar irradiance**,** seasonal rainfall, and frequent atmospheric dust, which significantly impact solar radiation and forecasting accuracy. These conditions make it an ideal site for evaluating solar irradiance forecasting models under real-world constraints.

Burkina Faso, a landlocked country in West Africa, spans the latitudes 09°02′–15°05′N and longitudes 02°02′E–05°03′W, and is subdivided into seventeen administrative regions. The terrain is mostly flat, with some elevated plateaus in the western region (Sawadogo, et al., 2024). According to the updated Köppen-Geiger climate classification, the extreme north presents a hot desert climate, the north shows a hot semi-arid climate, while the south and west exhibit a tropical savannah climate (Kottek et al., 2006). The Sudano-Sahelian zone, where Zagtouli is located, acts as a transitional area between the Sudanian and Sahelian zones, with mean annual rainfall between 600–900 mm and average temperatures ranging from 25 to 30 °C.

This climatic variability influences both solar energy production and vegetation cover. Plant diversity decreases from the Sudanian to the Sahelian zone (Heubes et al., 2013 ; Schmidt et al., 2017), and the landscape is dominated by a mosaic of savannas, with scattered dry forests, riparian forests, and woodlands.

Given its strategic location**,** operational data availability, and exposure to dynamic atmospheric conditions, the Zagtouli Solar Power Plant is an ideal case study for comparing the performance of numerical weather prediction (NWP) models, such as WRF-Solar, with data-driven machine learning approaches in three-day-ahead solar irradiance forecasting.

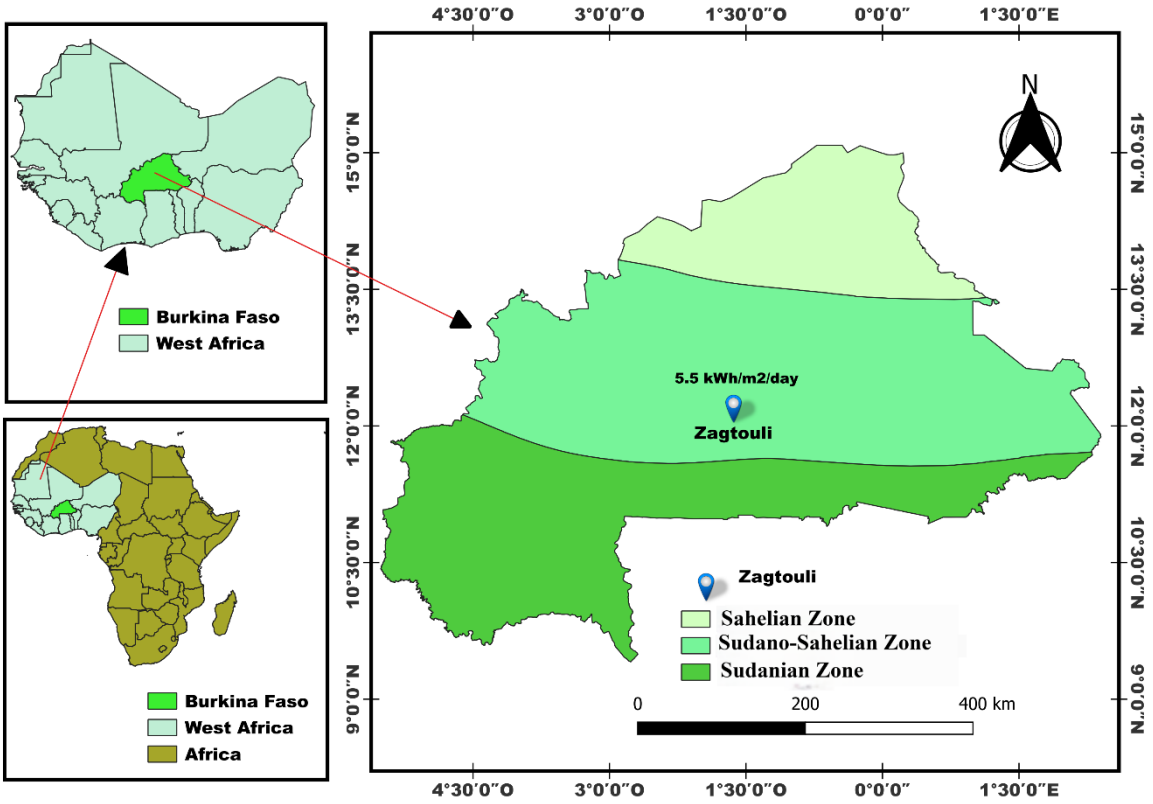

Figure 1: Map of study area with 5.5 kWh/m^2/day as GHI during a day.

2.2 Data

2.2.1 Ground-based measurements

The dataset used in this study was collected from the SONABEL (Société Nationale d'électricité du Burkina Faso) located in central of Burkina Faso at Zagtouli (Figure 1) (Zagtouli SONABEL, Burkina Faso, 12°30 N, 1°63 O, 327 m altitude) and spans the entire year of 2020. Measurements were recorded at 30-minute intervals. The variables collected are:

- Energy output (in megawatt-hours, MWh),
- GHI measured in watts per square meter (W/m²), and
- Ambient temperature measured in degrees Celsius (°C).

The station is located in the solar farm of SONABEL, at about 1 km of the main road leading to Bobo Dioulasso. These variables form the basis for analysing the relationship between meteorological conditions and energy production.

2.2.2 ERA5 Reanalysis data

For training the ML models, ERA5 Reanalysis data were used in this study. ERA5 is the fifth-generation reanalysis dataset produced by the European Centre for Medium-Range Weather Forecasts (ECMWF), offering significant improvements over its predecessor, ERA-Interim. With a horizontal grid spacing of approximately 31 km and 37 pressure levels ranging from 1000 hPa (surface) to 1 hPa, ERA5 is built on the advanced 4D-Var data assimilation system using cycle 41r2 of the Integrated Forecasting System (IFS) (Hersbach et al., 2020). It provides consistent global atmospheric reanalysis data from 1950 to the present, making it a reliable resource for climate monitoring, model evaluation, and various atmospheric studies (Ma & Wang, 2023; Dommo et al., 2022; Adeniyi, 2016). In this study, ERA5 hourly data, including surface and atmospheric pressure variables, were retrieved for the period spanning from 1 December 2018 to 31 December 2019 to drive the Initial and Lateral Boundary Conditions (ILBC) of the WRF-Solar model.

2.2.3 CAMS Datasets

To integrate aerosol into ML model's prediction, the Copernicus Atmosphere Monitoring Service (CAMS) data were used for this thesis. We used CAMS datasets to account for the direct effect of aerosol on radiation in the WRF-Solar model. The CAMS data uses the Integrated Forecasting System (IFS) developed by the European Centre for Medium-Range Weather Forecasts (ECMWF) to provide near-real-time forecasts and reanalysis of aerosols. IFS incorporates meteorological and satellite-based atmospheric data using a technique called 4D-VAR (four-dimensional variational data assimilation). Aerosol and chemical forecasts are produced twice daily at 00:00 UTC and 12:00 UTC, covering a five-day period. These forecasts include 56 reactive trace gases in the troposphere and stratospheric ozone, as well as seven types of aerosols: desert dust, sea salt, organic matter, black carbon, sulphate, nitrate, and ammonium (Christophe, 2019).

CAMS data are generated with a horizontal resolution of around 40 km (TL511) and 137 vertical layers spanning from the surface up to 0.01 hPa. Since 2015, forecast data have been available at 3-hour intervals (Inness et al., 2019). For this study, we retrieved 72-hour forecasts of aerosol optical depth (AOD) at the wavelength 550 nm for the year 2020, starting from 00:00 UTC each day, the period corresponding to each selected day for the different atmospheric conditions of this research.

2.2.4 ECWMF-HRES

We used the ECWMF-HRES as initial and lateral boundary conditions in the WRF-Solar model. The European Centre for Medium-Range Weather Forecasts (ECMWF) is a leading institution in global weather prediction, known for delivering reliable and advanced forecasts worldwide (Edwards, 2019). These forecasts are continually improved by integrating the latest observational data from satellites, weather balloons, and other sources. ECMWF provides several types of forecasts. For this study, we used the high-resolution forecast (HRES) data. HRES forecasts are generated using advanced numerical weather prediction (NWP) models that take into account a wide range of atmospheric variables and run on fine-resolution computational grids. This allows them to produce detailed and highly accurate single-forecast predictions.

HRES is considered ECMWF's most precise weather forecast product. With the latest updates to the Integrated Forecasting System (IFS) specifically the transition from cycle 43r3 to 45r1, forecast accuracy has improved further (Haiden et al., 2021), especially in tropical regions like West Africa. HRES forecasts are issued twice daily, based on observations collected at 00:00 and 12:00 UTC, and provide predictions up to 10 days ahead. The data are available at a temporal resolution of 3 hours. The HRES forecast uses an interpolated grid with a horizontal resolution of approximately 9 km and includes 137 vertical levels, with the model top set at around 0.01 hPa. For this study, we obtained 3-hourly data from 72-hour forecasts initialized at 00 UTC, covering all the essential surface and pressure-level variables needed to run WRF-Solar for the year 2020.

2.2.5 Model Inputs

The input variables used in the Machine Learning (ML)-based solar irradiance forecasting system were carefully selected to capture the key meteorological and environmental factors influencing surface solar radiation. The forecasting models developed using algorithms such as Support Vector Regression (SVR), Random Forest (RF), and LSTM relied on satellite-derived observations.

The selected features included:

- Longitude and latitude,
- Zonal and meridional wind components (u10, v10)**,**
- Maximum and minimum air temperature at 2 meters (Tmax, Tmin)**,**
- Temperature at 2 meters (T2m)

- Relative humidity**,**
- Precipitation**,**
- Total cloud cover**,**
- Surface pressure**,**
- Dew point temperature**,**
- Aerosol optical depth (AOD), and
- Wind speed**.**

These variables were chosen based on their established relevance in the literature for accurately predicting solar irradiance. For instance, cloud cover, humidity, and AOD are known to significantly affect solar radiation reaching the surface (Demir, 2025; Si et al., 2021; Szymszová et al., 2025). Temperature extremes and dew point relate to atmospheric stability, while wind components and speed are proxies for local air mass movement, which can influence cloud dynamics and aerosol dispersion (Bui et al., 2019; Voyant et al., 2017b).
The datasets had varying temporal resolutions (hourly, and 3-hourly) and spatial resolutions, depending on the source, allowing for flexible modelling across different forecast horizons.

2.2.6 Feature Description

Simulations are conducted using reanalysis data collected from ERA5, which provides data such zonal wind component (u10), meridional wind component (v10), temperature at 2 m (t2m), surface pressure(sp), maximum temperature at 2 m (mx2t), minimum temperature at 2 m (mn2t), dew point temperature at 2 m (d2m), total precipitation (tp), total cloud cover (tcc), sunshine radiation or GHI, total aerosol optical depth at 550 nm (aod550). The wind speed (ws) is calculated from the wind component, while the relative humidity (rh) is from the temperature at 2 m (t2m) and the dew point temperature (d2m). The referred data is from the city of Ouagadougou, Burkina Faso (12◦30 N, 1◦63 W). Temperatures are quite stable with a minimum of 22 ◦C and a maximum of 31 ◦C. The period covered by the database is from 1 January 2018 to 31 December 2019 in sampling intervals of 1 h. Table 1 shows all variables in the database.
Table 2: Input variables to forecast GHI using ML models.

Name	ShortName	Units
Latitude	lat	◦
Longitude	lon	◦
10 metre U wind component	u10	m s-1

10 metre V wind component	v10	m s-1
2 metre dewpoint temperature	d2m	˚C
2 metre temperature	t2m	˚C
Surface pressure	sp	hPa
Maximum temperature at 2 m	mx2t	˚C
Minimum temperature at 2 m	mn2t	˚C
Total precipitation	tp	mm
Total cloud cover	tcc	0-1
Global Horizontal Irradiance	ssrd	W/m²
Total aerosol optical depth at 550 nm	aod550	nm
wind speed	ws	m s-1
Relative humidity	rh	%

2.3 Methodology

In this section, we begin with the evaluation of WFR-SOLAR, the quality control of the data, followed by how the data are pre-processed, and then proceed to elaborate on four distinct models tailored for hourly solar radiation forecasting. These models encompass the WRF-Solar, Long Short-Term Memory, Random Forest, and Support Vector Regression. Finally, the evaluation of some metrics.

2.3.1 Quality Control

Figure 2 shows a comprehensive process for handling the missing values in the dataset. This process consists of steps, techniques, and equations to ensure data quality. These steps help improve the integrity, accuracy, and reliability of the station data used in this study.

The observational data was used and have a temporal resolution 30 min. The following steps are used to compute the instantaneous hourly data:

1. The missing date is added and the value for GHI is marked missed if that date is not in the time series.
2. During nighttime, GHI values are attributed to 0, even if they are missed.
3. We selected hourly instantaneous GHI values. If this value is missed, we process to the nearest time to the considered hour.

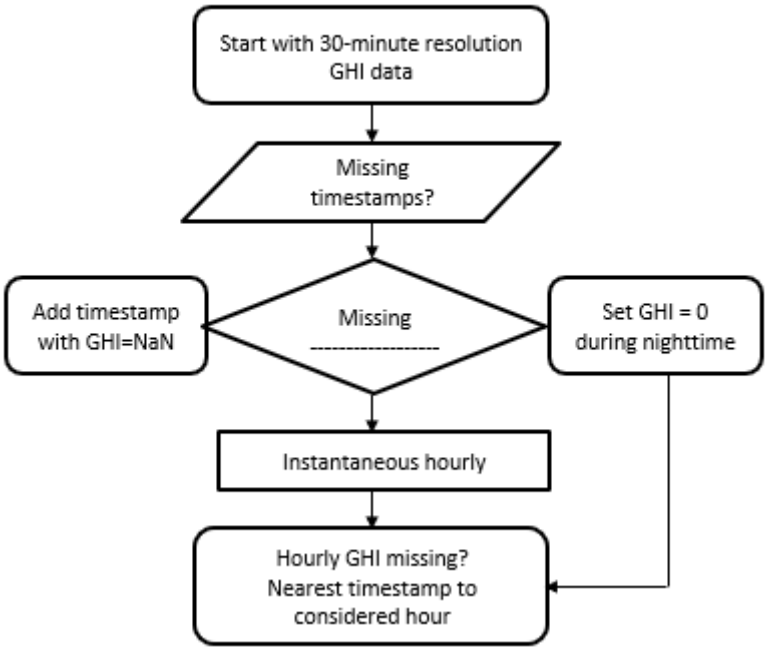

Figure 2: Data handling flowchart

The second step was to categorize the different daily atmospheric conditions based on the clearness index. For that, we calculated the daily average (K_t) for all days in the year 2020 from the observation. The clearness index (K_t) quantifies how much extraterrestrial solar radiation is reduced by atmospheric elements such as clouds and aerosols, effectively indicating the transparency of the Earth's atmosphere to solar radiation (Akhlaque et al., 2009; Augustine & Nnabuchi, 2009; Poudyal et al., 2012; Liu & Jordan, 1960; Soneye, 2021).

The K_t is defined as the ratio of surface solar irradiance (GHI) to extraterrestrial solar irradiance G_0 and is expressed as follows:

$$K_t = \frac{GHI}{G_0} \quad (1)$$

The following equation helped to obtain the daily extraterrestrial radiation G_0 ($MJ/m^2/day$) is obtained (Allen et al. 1998):

$$G_0 = \frac{24(60)}{\pi} G_{SC} d_r [\omega_s sin(\varphi) sin(\delta) + cos(\varphi) cos(\delta) sin(\omega_s)], \quad (2)$$

where G_{SC} is the solar constant (0.0820 $MJ/m^2/min$), d_r is the inverse relative distance for Earth–Sun (rad), ω_s is the sunset hour angle (rad), φ is the latitude of the location (rad), and δ the solar declination (rad).

From the hourly GHI, the daily GHI is determined if there is no single missing value. In previous studies, the clearness index has been used to categorise sky conditions. For instance, Du et al. (2022) classified the sky conditions using K_t to validate clear-sky and cloudy conditions using

MERRA-2 hourly dataset over China. However, the values of K_t set to define cloudy and clear skies in China might be different from West Africa. This study highlights clear-sky when $K_t \geq 0.6$ and cloudy-sky when $0.12 \leq K_t < 0.35$. From previous studies over West Africa (Soneye, 2021; Kuye & Jagtap, 1992), these values were taken.

Moreover, the occurrence of high-aerosol days is identified using the 99th percentile of AOD550, and from this, four days were selected; while the mixed cloudy and high aerosol days, the days that meet the condition of cloudy and high aerosol days, were considered. Figure 3 illustrates the threshold defined to categorise each sky conditions day.

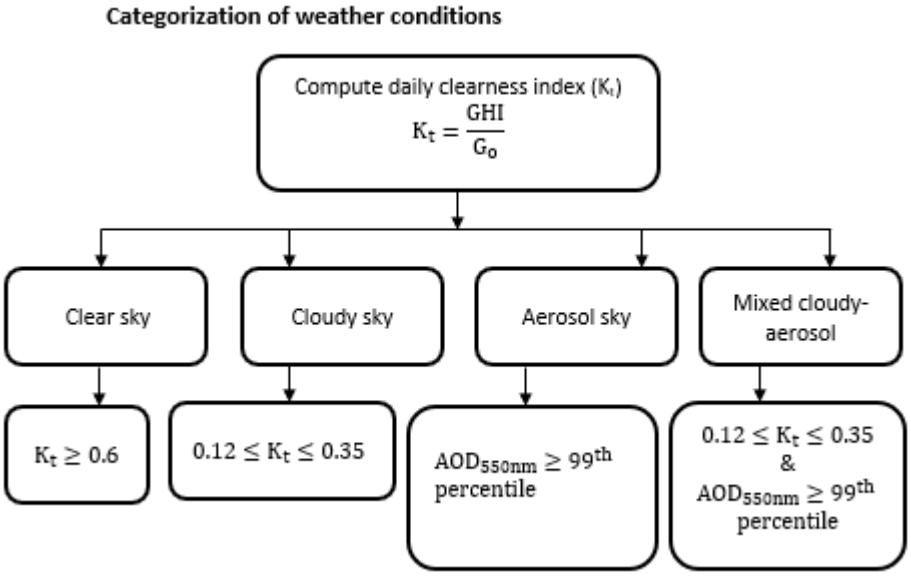

Figure 3: Categorisation of sky-conditions day based on clearness index K_t.

The hourly data obtained, have undergone other analysis. The extremely rare limit (and the physically possible limit (4) of GHI measurements are defined according to the Baseline Surface Radiation Network (BSRN) guidelines (BSRN, 2021).

$$-2\ \mathrm{W}/m^2 < \mathrm{GHI} < I_0 * 1.5 * \cos(SZA)^{1.2} + 50\ \mathrm{W}/m^2 \quad (3)$$

$$-4\ \mathrm{W}/m^2 < \mathrm{GHI} < I_0 * 1.5 * \cos(SZA)^{1.2} + 100\ \mathrm{W}/m^2 \quad (4)$$

I_0 represents the solar constant and is 1367 W/m2 given by H. Li et al. (2011), and SZA denotes the solar zenith angle. For the BSRN closure tests, analyses were limited to cases where SZA < 80° to account for the seasonal variation in sunrise and sunset times over the region.

Figure 4 illustrates the quality control of the hourly GHI based on the Eqs. (3) and (4). The physically possible limit is in red and the extremely rare limit in blue. The black dots indicate the hourly GHI measurements.

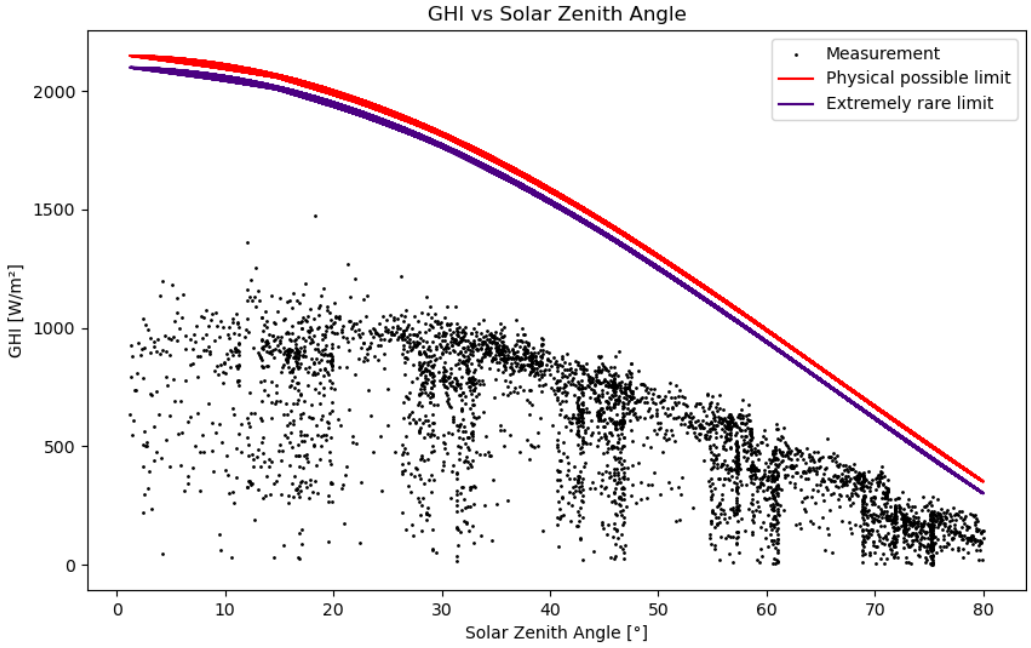

Figure 4: Quality control of the station based on the Baseline Surface Radiation Network (BSRN).

Most data points that fall outside the BSRN-defined limits occur within the solar zenith angle (SZA) range of 75° to 80°. This range typically corresponds to early morning (7:00–8:00 AM) and late afternoon (5:00–6:00 PM) hours, depending on this region. Fortunately, no data point has fallen outside BSRN-defined limits.

In the final step, outlier detection was used to identify erroneous GHI values in the dataset. Specifically, this study focused on far outliers in the observations, calculated using the method proposed by Younes et al. (2005) as follows:

$$\text{Upper outlier limit} = \text{3rd quartile} + 3 * (\text{3rd quartile} - \text{1st quartile}) \quad (5)$$

$$\text{Lower outlier limit} = \text{3rd quartile} - 3 * (\text{3rd quartile} - \text{1st quartile}) \quad (6)$$

The outlier analysis was based on the daily clearness index (Kt), and data points falling outside the upper and lower limits were excluded from the analysis.

Figure 5 illustrates the interquartile range (shaded in grey), along with the upper outlier limit (indicated by red dot) and the lower outlier limit (indicated by green dot) for the AWS (Automatic Weather Station) data.

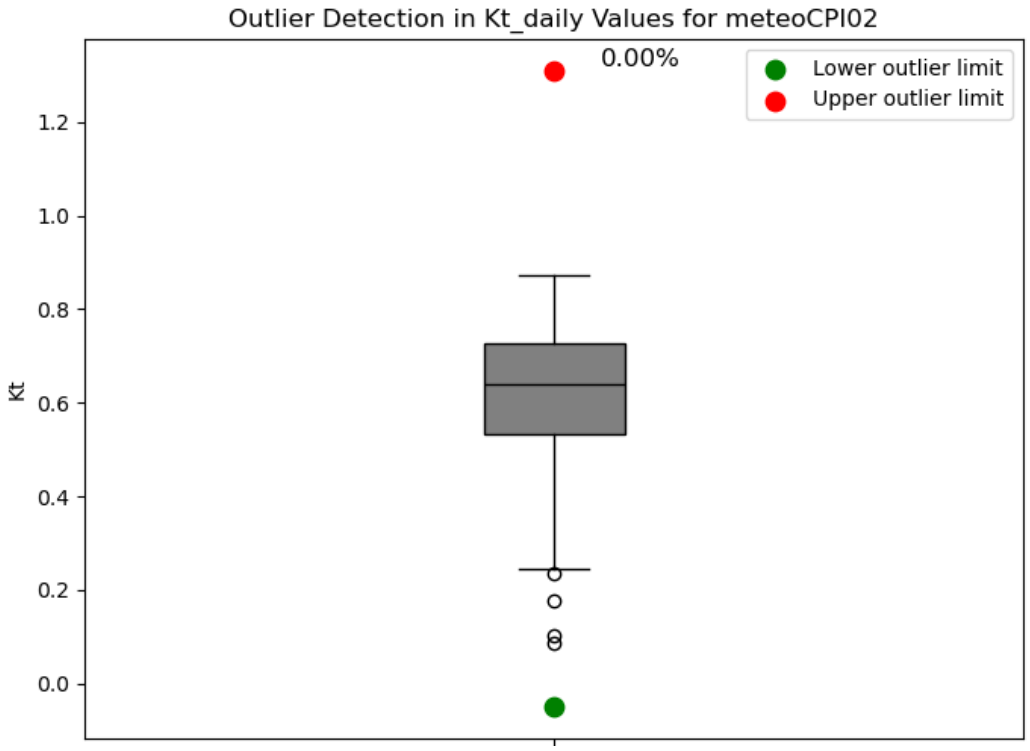

Figure 5: Boxplot of the daily clearness index (Kt) of the AWS data for the year 2020.

In summary**,** the data seems to be of good quality when validated against physical limits and statistical behaviour. The GHI values are within theoretical predicted limits for all solar zenith angles, indicating compliance with accepted physical laws (Figure 4). Similarly, the Kt values also remain within reasonable limits, with nothing to indicate extreme anomalies or aberrant behaviour. The existence of a small percentage of low-end outliers (Figure 5) is to be anticipated and is rather more likely to be the result of natural atmospheric variability than failure of the

sensor or data corruption issues. The solar radiation data can therefore be considered valid and fit for follow-on modelling or analytical work.

Following the above analyses that confirmed the data quality for the study, and the time that we have to conduct the study and simulate the WRF-Solar because it has a computationally cost, we randomly selected 10 clear-sky days, 10 cloudy days, 4 high-aerosol days, and 3 days with mixed cloudy and high-aerosol conditions within the year 2020. The selected days are summarized in Table 3.

Table 3: Selected days based on weather type.

Sky - conditions	**Selected days**
Clear days	2020-01-11 2020-11-20 2020-06-29 2020-12-13 2020-10-12 2020-12-21 2020-11-18 2020-04-06 2020-11-14 2020-11-11
Cloudy days	2020-03-24 2020-09-05 2020-08-25 2020-04-15 2020-07-19 2020-06-09 2020-08-08 2020-05-28 2020-09-06 2020-08-27
Aerosol - days	2020-03-04 2020-04-19 2020-04-20 2020-04-21
Cloudy - aerosol days	2020-03-24 2020-04-15 2020-06-09

2.3.2 WRF-Solar Setup

In this study, we applied the WRF-Solar model (version 4.2.1) with a physics configuration tailored for high-resolution solar irradiance forecasting over a specific West African subregion. While the meteorological and environmental inputs such as initial and boundary conditions from ECMWF-HRES, aerosol data from CAMS, land use, and topographic datasets remained identical to those used in the optimized WRF-Solar configuration presented by Sawadogo, et al. (2024), the key adaptation in our approach is the redefinition of the simulation domain to better represent local atmospheric dynamics.

The model was set up using a two-domain, one-way nested configuration. The outer domain (D1) extends from -2.005 S to 25.889 N and -18.306 W to 15.046 E at 15 km resolution (244 x 211 grid points), and the inner domain (D2) covers 8.802 S to 16.035 N and -6.091 W to 3.380 E at 3 km resolution (346 x 271 grid points), as presented in Figure 6.

00 UTC daily forecasts were initialized from ECMWF-HRES and extended 72 hours ahead for each of selected day of 2020. The forecast cycle generates three overlapping forecast days Lead 0 (current day), Lead 1 (next day) and Lead 2 (day after next), enabling continuous coverage.

The physical parameterizations implemented in our WRF-Solar setup reflect a deep understanding of radiative and atmospheric processes that influence solar radiation. The shortwave and longwave radiative transfer were handled using the RRTMG (updated Rapid Radiative Transfer) scheme, with the shortwave component enhanced by aerosol interactions via the RRTMG-AERO module. This allowed the model to account for direct aerosol effects on solar radiation, incorporating dynamic AOD_{550} values updated every three hours from CAMS. Radiative properties such as single scattering albedo and asymmetry factor were computed using aerosol type and relative humidity profiles.

Microphysical processes were represented using the aerosol-aware Thompson scheme, allowing for feedback between aerosol loading and cloud microphysics critical for accurate GHI simulation. The land surface was modelled with the Noah Land Surface Model, while the MYNN (Mellor–Yamada–Nakanishi–Niino) scheme was used for Planetary Boundary Layer (PBL) processes to ensure realistic surface–atmosphere energy exchanges. Shallow cumulus processes were captured using Deng's shallow convection parameterization, a scheme favoured in WRF-Solar for its ability to simulate sub-grid scale cloud–radiation feedback. Cumulus convection was deactivated in both domains in favour of this shallow scheme, which employs a mass-flux approach with prognostic cloud fraction and liquid/ice content equations. To accelerate radiative computations while maintaining accuracy, we activated the Fast All-sky

Radiation Model for Solar applications (FARMS). We used the hourly gridded GHI output (SWDOWN2) as our main irradiance variable for model evaluation. The simulation used 45 vertical terrain-following eta levels from the surface (1000 hPa) up to 50 hPa, capturing fine-scale atmospheric structure necessary for reliable irradiance modelling. Overall, the model configuration mirrors optimized practices in solar forecasting while introducing geographic specificity that enhances its relevance for the target study area.

Table 4 below summarizes the key physical parameterizations adopted in this WRF-Solar configuration.

Figure 6: WRF-Solar modelling domains.

Table 4: WRF-Solar model setup, parameterizations and data used.

Physics	RRTMG	RRTMG_AERO
Radiation SW	RRTMG	RRTMG + aerosols
Radiation LW	RRTMG	RRTMG
Microphysics	Thompson	Aerosol-aware Thompson
Land surface	Noah land surface model	
Planetary boundary layer	MYNN	
Shallow cumulus	Deng cumulus	
FARMS	Activated	

2.3.3 Data Preprocessing

To develop the solar irradiance forecasting models, meteorological data from ERA5 spanning the years 2018 and 2019 were used exclusively for training. These two years provided the historical input needed to learn the relationship between meteorological variables and global horizontal irradiance (GHI). Once the models were trained and evaluated on this training data, they were saved for later use.

For testing and prediction, only selected days from the year 2020 categorized by atmospheric conditions as shown in Table 3 were used. These days were excluded from the training phase and served solely to assess the generalization capacity of the saved models. Corresponding observed GHI data from SONABEL for these specific days were also used to validate the accuracy of the forecasts.

Before model training, input features were normalized using Min-Max scaling to ensure consistent data distribution and improve model convergence. After training, model performance was first evaluated using standard metrics such as RMSE and MAE on the training/validation set (2018–2019) to ensure model quality before deployment.

a. Data normalization

Data normalization is a critical preprocessing step required before applying any DL and some ML models, as it ensures that the influence of differing feature attribute scales is minimized. This process helps accelerate the convergence of the model during training and enhances its predictive accuracy. In this study, we adopt the min-max normalization technique to scale the data to a uniform range. The normalized value z_n is calculated using the following formula:

$$z_n = \frac{x - x_{min}}{x_{max} - x_{min}} \quad (7)$$

where x represents the original data value, x_{min} is the minimum value, and x_{max} is the maximum value in the dataset. This transformation ensures that all input features lie within a common scale, typically between 0 and 1, which is essential for the effective performance of deep learning algorithms.

2.3.4 Machine Learning Models

Each forecasting methodology is described shortly in this paragraph: Random Forest, Support Vector Machine (SVM) and Long Short-Term Memory (LSTM). Random Forest and Support Vector Machine (SVM) belong to the family of single or traditional ML models, while the LSTM belongs to Artificial Neural networks (ANN) in the family of Deep Learning (DL) models.

a. Random Forest (RF)

The random forest method is an improved model of bagging regression trees (Voyant et al., 2017; Zamo et al., 2014; Prasad et al., 2006; Yu et al., 2017) and used to avoid overfitting. The binary RT method works by repeatedly dividing the data into two groups based on specific rules and thresholds (Zamo et al., 2014). It builds a set of decision rules using predictor variables (Breiman et al., 1984; Verbyla, 1987; Linda A. Clark, 1992), aiming to split the data into smaller, more uniform groups. At each step, it selects one predictor and a threshold that best increases the similarity of values within the resulting two groups (Prasad et al., 2006). This process continues recursively, dividing each group into two subgroups. In the end, each final group (or "leaf") predicts the average value of its members. The method initially grows a large tree, which is then pruned, often using cross-validation to avoid overfitting and find the optimal tree size (Therneau & Atkinson, 1997).

Breiman (1996) introduced the idea of improving prediction stability by averaging the outputs of multiple decision trees. To do this without requiring separate datasets, he used randomly drawn samples (with replacement) from the original data, a technique known as bagging (short for bootstrap aggregating). Later, he enhanced this method by adding a random selection of predictor variables at each split (Breiman, 2001; Breiman, 2002; Zamo et al., 2014), resulting in the Random Forest (RF) algorithm.

In a random forest, each tree is trained on a different random sample, and predictor subsets are chosen randomly at each split. This added randomness improves robustness and reduces

overfitting. Finally, the predictions from all trees are averaged to produce the final result. Random Forests are widely regarded as one of the most powerful machine learning models for forecasting and will be used in this study. For more details on regression tree-based methods, see the references in this section.

Table 5: Parameters used for RF model.

Parameter	Value / Description
Model Type	RandomForestRegressor
n_estimators	100 (number of trees in the forest)
random_state	42 (ensures reproducibility)
n_jobs	-1 (uses all available cores for training)

b. Support Vector Machine (SVM)

Support Vector Regression (SVR) is a supervised machine learning method that extends the Support Vector Machine (SVM) framework to handle regression tasks (Heimo, 2012). It operates by fitting a hyperplane within a predefined margin of tolerance, defined by upper and lower bounds, and relies on support vectors to determine the optimal model parameters, as shown in Equation (8).

$$Y = f(x) = \omega \cdot \phi(x) + b \quad (8)$$

Where x represents the independent variable, ω and b are the weight vector and bias term, respectively, and $\phi(x)$ denotes the nonlinear mapping function that transforms the input data into a higher-dimensional feature space.

When working with multidimensional datasets, the target variable Y can have infinitely many possible values, making direct prediction complex. To manage this, SVR introduces a tolerance margin ε, within which errors are ignored, effectively simplifying the optimization problem. This leads to the following formulation

(9).

$$min\ \omega\frac{1}{2}\omega^2 + C\sum_{i=1}^{l}(\xi_i + \xi_i^*),$$

Subject to (9)

$$\begin{cases} y_i - \omega^T x_i - b \leq \varepsilon + \xi_i \\ \omega^T x_i + b - y_i \leq \varepsilon + \xi_i^* \\ \xi_i, \xi_i^* \geq 0 \end{cases}$$

Where C is a positive regularization parameter that controls the trade-off between the model's flatness and the allowable prediction error. The term ω represents the weight vector, while ξ_i and ξ_i^* are slack variables that account for deviations beyond the ϵ-insensitive zone. These slack variables help minimize the prediction error outside the tolerated margin.

To solve this nonlinear regression problem efficiently, the optimization can be reformulated in its dual form using Lagrange multipliers. This dual representation also incorporates kernel functions to handle non-linear relationships in the data. The dual formulation is given in Equation (10):

$$min: \frac{1}{2}\sum_{i,j=1}^{n}(\alpha_i + \alpha_i^*)\,(\alpha_j + \alpha_j^*)k(x_i.x_j) + \varepsilon\sum_{i=1}^{n}(\alpha_i + \alpha_i^*) - \sum_{i=1}^{n} y_i(\alpha_i + \alpha_i^*) \quad (10)$$

subject to

$$\begin{cases} \sum_{i=1}^{n}(\alpha_i + \alpha_i^*) = 0 \\ 0 \leq \alpha_i, \alpha_i^* \leq C \\ \text{for } i = 1, 2, \ldots, n \end{cases}$$

Where α_i and α_i^* denote the Lagrange multipliers, and $k(x_i.x_j)$ represents the kernel function used to handle the nonlinear regression task. Among the various kernel options, the Radial Basis Function (RBF) kernel was chosen in this study due to its flexibility and strong ability to model complex, nonlinear relationships between input and output variables. The RBF kernel is defined as follows (11):

$$k(x_i.x_j) = exp\left(-\gamma|x_i - x_j|^2\right) \quad (11)$$

Where γ is a tunable kernel parameter that controls the width of the RBF kernel, and $|x_i - x_j|^2$ denotes the squared Euclidean distance between the input vectors x_i and x_j. A

smaller γ value implies a smoother decision function, while a larger γ allows the model to capture more complex patterns.

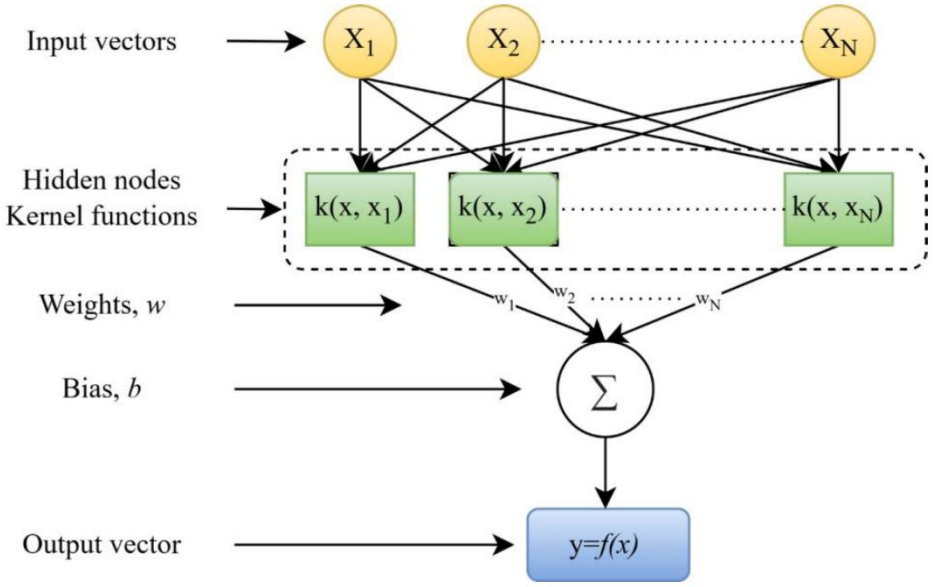

Figure 7: SVR Structure.

Finally, the SVR decision function, which is used to predict the output for a new input x, is given by (12):

$$f(x) = \sum_{i=1}^{n} (\alpha_i + \alpha_i^*) k(x_i . x_j) + b \quad (12)$$

In this thesis, the configuration of SVR model used and some meanings are summary in Table 6.

Table 6: Parameters used and their description for SVR model.

Section	Parameter	Value / Description
Hyperparameter Tuning	GridSearchCV	Performs exhaustive search over specified parameters using 3-fold cross-validation
	param_grid['kernel']	['rbf', 'poly'] – tested RBF and polynomial kernels
	param_grid['C']	[1, 10, 100] – regularization strength
	param_grid['epsilon']	[0.001, 0.01, 0.1] – insensitive loss function margin
	cv	3 – number of cross-validation folds
	scoring	neg_mean_squared_error – performance metric used during grid search
	n_jobs	-1 – uses all processors for parallel training
	verbose	1 – prints progress of GridSearch

c. Long Short-Term Memory (LSTM)

LSTM (Long Short-Term Memory) is a type of recurrent neural network (RNN) designed to overcome the short-term memory limitations of traditional RNNs (Hochreiter, S., & Schmidhuber, 1997) (Hochreiter, S., & Schmidhuber, 1997). It can retain important information over longer periods, making it well-suited for time series tasks. Each LSTM cell includes three key components: the forget gate, which decides what past information to keep; the input gate, which adds relevant new information; and the output gate, which determines the next hidden state. The internal structure of an LSTM cell is illustrated in Fig. 1.

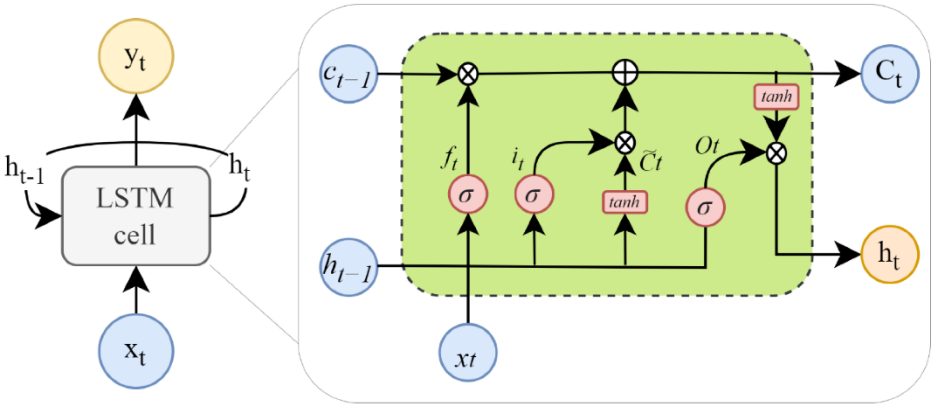

Figure 8: LSTM architecture

The forget gate in an LSTM cell decides which information from the past should be kept or discarded. It takes the previous hidden state (h_{t-1}) and current input (x_t), combines them, applies a weight matrix W_f, adds a bias b_f, and passes the result through a sigmoid function:

$$f_t = \sigma\left(W_f \cdot [h_{t-1}, x_t] + b_f\right) \quad (13)$$

Values close to 0 mean "forget," while values close to 1 mean "retain."

Next, the input gate controls how much new information is added to the cell state. It also uses the current input and previous hidden state, applies weights and a sigmoid activation:

$$i_t = \sigma(W_i \cdot [h_{t-1}, x_t] + b_i) \quad (14)$$

A value near 1 means the information is important.

To generate the candidate cell state ($\bar{c}_t$), the same inputs (x_t) go through the $tan\,h$ function, producing values between –1 and 1 that represent new information. This candidate state is then scaled by the input gate's output to decide what to add to the cell state.

$$\bar{c}_t = tan\,h\,(W_c \cdot [h_{t-1}, x_t] + b_c) \quad (15)$$

The updated cell state c_t is then computed by combining the old cell state, scaled by the forget gate, and the candidate state, scaled by the input gate:

$$c_t = f_t * c_{t-1} + i_t * \bar{c}_t \quad (16)$$

This allows the LSTM to retain relevant information over time.

The output gate decides what information from the cell state should be output. It again processes the input and previous hidden state:

$$o_t = \sigma(W_o \cdot [h_{t-1}, x_t] + b_o) \quad (17)$$

Finally, the new hidden state (which is also the LSTM cell's output) is computed by applying a $tan\,h$ activation to the updated cell state and scaling it with the output gate:

$$h_t = o_t * tan\,h\,(c_t)) \quad (18)$$

Where x_t is current input; $h_{t-1}$the previous hidden state; c_{t-1}: previous cell state; σ: sigmoid function; $tan\,h$: hyperbolic tangent function; W_*, b_* are weight matrices and biases for each gate; f_t, i_t, o_t :forget, input, and output gates; $\bar{c}_t$: candidate new information, c_t: new cell state and h_t: new hidden state/output.

The parameters used in LSTM model and their descriptions are summarized in Table 7Table 7.

Table 7: LSTM model configurations.

Parameter	Value/Description
LSTM Units	64
Return Sequences	False
Dense Layer 1	32 units, ReLU activation
Optimizer	Adam
Loss Function	Mean Squared Error (MSE)
Epochs	30
Batch Size	16
Callback	EarlyStopping (patience=10, restore_best_weights=True)

2.3.5 Evaluation Metrics

To assess the accuracy of model predictions, some error metrics are used and provide quantitative evaluations of the discrepancy between the forecasted and observed values of global horizontal irradiance (GHI). In this study, we employed several commonly used statistical metrics: the Root Mean Square Error (RMSE) (Eq. *(19)*) and the Mean Absolute Error (MAE) (Eq*(20*) to measure the average magnitude of forecast errors. To account for scale and provide relative performance insights, we also computed the Normalized RMSE (nRMSE) (Eq. *(21*) and the Normalized MAE (nMAE) (Eq. *(22*). In addition, we used coefficient of determination (R^2) (Eq. *(23*) which tells about the forecasted and real value's correlation, and the Index of Agreement (IOA) (Eq. *(24*) to assess model agreement. Willmott (1981) on the validation of model, use the value of IOA ranging from 0 to 1 in which 1 means perfect agreement while 0 means no agreement.

The different statistical metrics are expressed as follows:

$$RMSE = \left[\frac{1}{N}\sum_{i=0}^{N}(P_i - O_i)^2\right]^{\frac{1}{2}} \quad (19)$$

$$MAE = \frac{1}{N}\sum_{i=0}^{N}|P_i - O_i| \quad (20)$$

$$nRMSE = \left[\frac{RMSE}{max(O) - min\,(O)}\right] * 100 \quad (21)$$

$$nMAE = \left[\frac{MAE}{max(O) - min\,(O)}\right] * 100 \quad (22)$$

$$R^2 = 1 - \frac{\sum(O_i - P_i)^2}{\sum\left(O_i - \underline{O}\right)^2} \quad (23)$$

$$IOA = 1 - \frac{\sum_1^n P_i - O_i}{\sum_{i=1}^n \left(|P_i - O_i||O_i - \underline{O}|\right)^2} \quad (24)$$

where P_i is the forecasted value, O_i the observation data at timestep i, $\underline{O}$ the mean of the observation, and n is the number of data points used for comparison. $max(O)$ and $min(O)$ are the maximum and minimum value of the observations.

In addition to the standard evaluation metrics, a skill score (denoted as *s*) was incorporated to assess the forecast verification performance. The skill score provides a quantitative measure of the relative accuracy between two forecasting systems, with one system designated as the reference(Murphy, 1988). It enables an objective comparison by indicating the degree to which the evaluated forecast improves upon (or degrades from) the reference forecast.

s can be based on some statistical metrics, but RMSE is commonly used in solar energy forecasting (Yang et al., 2020; Blaga et al., 2019; Yang, 2018). Thus, s is expressed as:

$$s = 1 - \frac{RMSE_{(f,x)}}{RMSE_{(r,x)}} \quad (25)$$

where f, r, and x denote forecasts of interest, reference forecasts, and observations, respectively. When $s > 0$, it means that the forecast is better than the reference forecast, while and $s < 0$ indicates that the forecast performs worse than the reference forecast. A value of $s = 0$ implies that the forecast's performance is equivalent to that of a reference forecast.

Reference forecasts can be generated using either the persistence method, which assumes that current conditions will remain unchanged, or the climatology method, which relies on long-term historical averages. However, for enhanced forecast performance, an optimal convex combination of both methods is recommended, particularly in solar energy applications (D. Yang, 2018) and has been strongly advocated by several studies (D. Yang et al., 2020).

Accordingly, to this study, we adopted the persistence model to construct the reference forecast.

Chapter 3: Results and discussion

In this section, we present the forecasting results of the WR-Solar model against ML models.

3.1 Characterizations of aerosol

Figure 9 displays the spatial distribution of AOD at 550 nm over Burkina Faso and surrounding regions on four specific dates: 04 March, 19 April, 20 April, and 21 April 2020. Each subfigure highlights daily mean in aerosol loading using a colour scale, where red shades indicate high aerosol concentration and blue shades represent low levels. On 04 March 2020, elevated AOD values are concentrated over the north-central region, with values reaching up to 1.2, suggesting the presence of Saharan dust transported into the area (Haywood et al., 2008). The southern part remains relatively clearer, indicating lower aerosol presence. On 19 April 2020, aerosol concentrations intensify across the northern and northeastern regions, with values climbing up to 1.6. This reflects a significant aerosol event likely influenced by regional biomass burning (Kaiser et al., 2012) or long-range dust transport. The most pronounced aerosol episode occurs on 20 April 2020, where AOD values exceed 2.0, particularly in the northwestern areas. This suggests a strong Saharan dust intrusion (Prospero et al., 2002), possibly combined with local and regional biomass burning sources. By 21 April 2020, aerosol levels slightly decrease but remain high, especially in the northern and eastern regions, with values ranging between 0.4 and 1.2. The southern zone consistently shows lower AOD across the days, indicating less aerosol burden. Overall, these plots demonstrate a clear north-to-south gradient in aerosol distribution and underline the impact of both Saharan dust and biomass burning on aerosol variability in Burkina Faso during the dry season (Ginoux et al., 2001; Haywood et al., 2008).

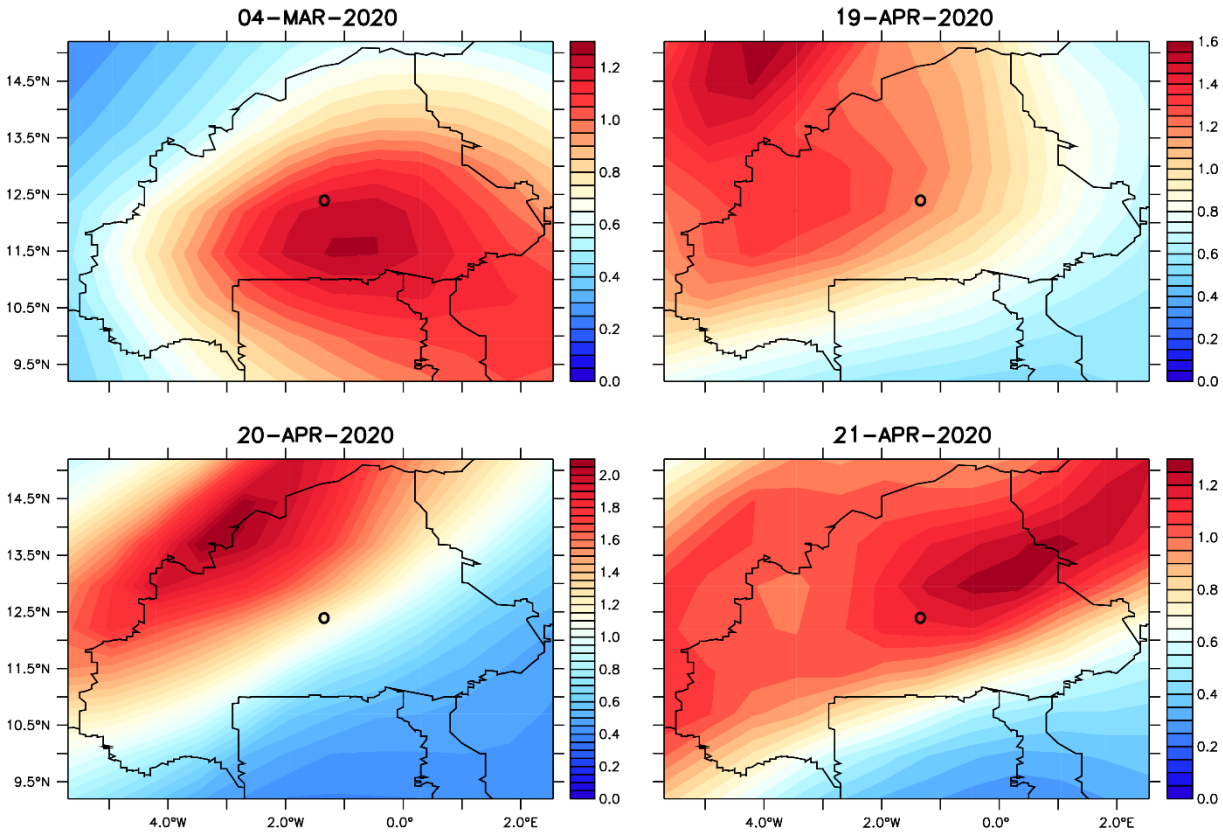

Figure 9: Spatial distribution of daily aerosol optical depth at 550 (AOD550) from CAMS reanalysis data for the year 2020. The circle indicates the Zagtouli PV Plant location.

3.2 WRF-Solar Model Performance Against Observations

3.2.1 Scatter plot.

The performance of the WRF-Solar model is evaluated under four distinct atmospheric conditions as Clear Sky**,** Cloudy Sky**,** Aerosol Sky**,** and Cloudy-Aerosol Sky over three prediction horizons: Lead 0, Lead 1, and Lead 2. It varies according to the sky conditions and lead time. The scatter plots in Figure 10 shows the relationship between observed and predicted solar irradiance values, with density indicated by colour. Several performance metrics are used to assess accuracy, including RMSE**,** nRMSE**,** MAE**,** nMAE**,** R^2**,** and IOA.

Under clear sky conditions, the WRF-Solar demonstrates excellent performance, with high predictive accuracy and strong correlations across all forecast lead times Lead 0 (Figure 10(a)) yields the most accurate results, achieving an RMSE of 69.0 W/m², a coefficient of determination (R^2) of 0.92, and an index of agreement (IOA) of 0.98. Although accuracy decreases slightly with increasing lead time. However, the model's performance remains robust. For Lead 1 (Figure 10 (b)), the RMSE increases to 121.9 W/m² and R^2 declines to 0.75, while Lead 2 (Figure 10 (c)) records an RMSE of 155.8 W/m² and an R^2 of 0.62.

Under cloudy conditions, the model's performance deteriorates considerably. At Lead 0 (Figure 10 (d)), accuracy is particularly poor, with an RMSE of 354.0 W/m², an R^2 of -2.92, and an IOA of 0.55. Slight improvements are observed for Lead 1 (Figure 10 (e)), with an RMSE of 281.4 W/m² and R^2 of -0.05, and for Lead 2 (Figure 10 (f)), with an RMSE of 303.7 W/m² and R^2 of -0.03. This poor performance is consistent with previous findings that cloud variability presents a major challenge in solar irradiance forecasting (Inman et al., 2013; Sawadogo et al., 2024; X. Zhou et al., 2024).

Under aerosol conditions, the model exbibits moderately good performance. Lead 0 (Figure 10 (g)) and Lead 1 (Figure 10 (h)) yield R^2 values of 0.94 and 0.67, respectively, indicating reasonable predictive capability. Even at Lead 2 (Figure 10 (i)), the model retains an R^2 of 0.76, suggesting aerosol effects are more predictable than clouds due to their slower spatiotemporal variability (Perez et al., 2016). The RMSE values range from 138.1 to 171.2 W/m² across the forecast horizons, further supporting the model's consistent performance under aerosol-laden conditions. WRF-Solar is moderately effective under high aerosol concentrations, maintaining decent accuracy and consistency.

Under cloudy-aerosol sky conditions, performance varies markedly across leads. At Lead 0 (Figure 10 (j)), predictive accuracy is extremely poor, with an RMSE of 388.0 W/m² and R^2 of -4.36. Lead 1 (Figure 10 (k)) shows some improvement with $R^2 = 0.57$. Interestingly, Lead 2 (Figure 10 (l)) improves significantly ($R^2 = 0.94$; RMSE = 65.9 W/m²), indicating possible stabilization of atmospheric conditions over longer time horizons (Coimbra et al., 2013).

Globally, the WRF-Solar model performs best under clear-sky conditions because its radiative transfer schemes are well-calibrated to simulate direct solar radiation without significant atmospheric interference. Several studies, such as Jimenez et al. (2016) and Lara-Fanego et al. (2012), show that = (NWP models like WRF-Solar can effectively capture solar irradiance in cloud-free environments, where the atmosphere behaves more predictably and inputs like aerosols and cloud microphysics have minimal impact. Nevertheless, under cloudier conditions, the model's accuracy declines due to the complexity and variability of cloud formation, movement, and optical properties. These are harder to model and forecast accurately, especially over short lead times. According to J. Yang et al. (2022),cloud representation remains a major source of uncertainty in solar irradiance forecasting. Aerosols introduce moderate error because, while their effect on radiation is less variable than clouds, they still scatter and absorb solar radiation, especially in polluted or dusty regions (West Africa). Models like WRF-Solar include aerosol modules, but their accuracy depends on high-resolution and up-to-date aerosol data

(Thaker & Höller, 2023). The most challenging scenario is a combination of clouds and aerosols, which interact in complex ways (aerosols may modify cloud albedo or lifetime). These nonlinear aerosol-cloud-radiation interactions are poorly captured in most NWP models, including WRF-Solar, leading to compounded errors (Zhang et al., 2010; Tuccella et al., 2019). Lastly, forecast accuracy generally decreases with increasing lead time, due to growing uncertainties in meteorological conditions. However, for mixed-sky (cloudy + aerosol) conditions, it is possible that Lead 2 (Figure 10) outperforms Lead 1 (Figure 10) due to random variations.

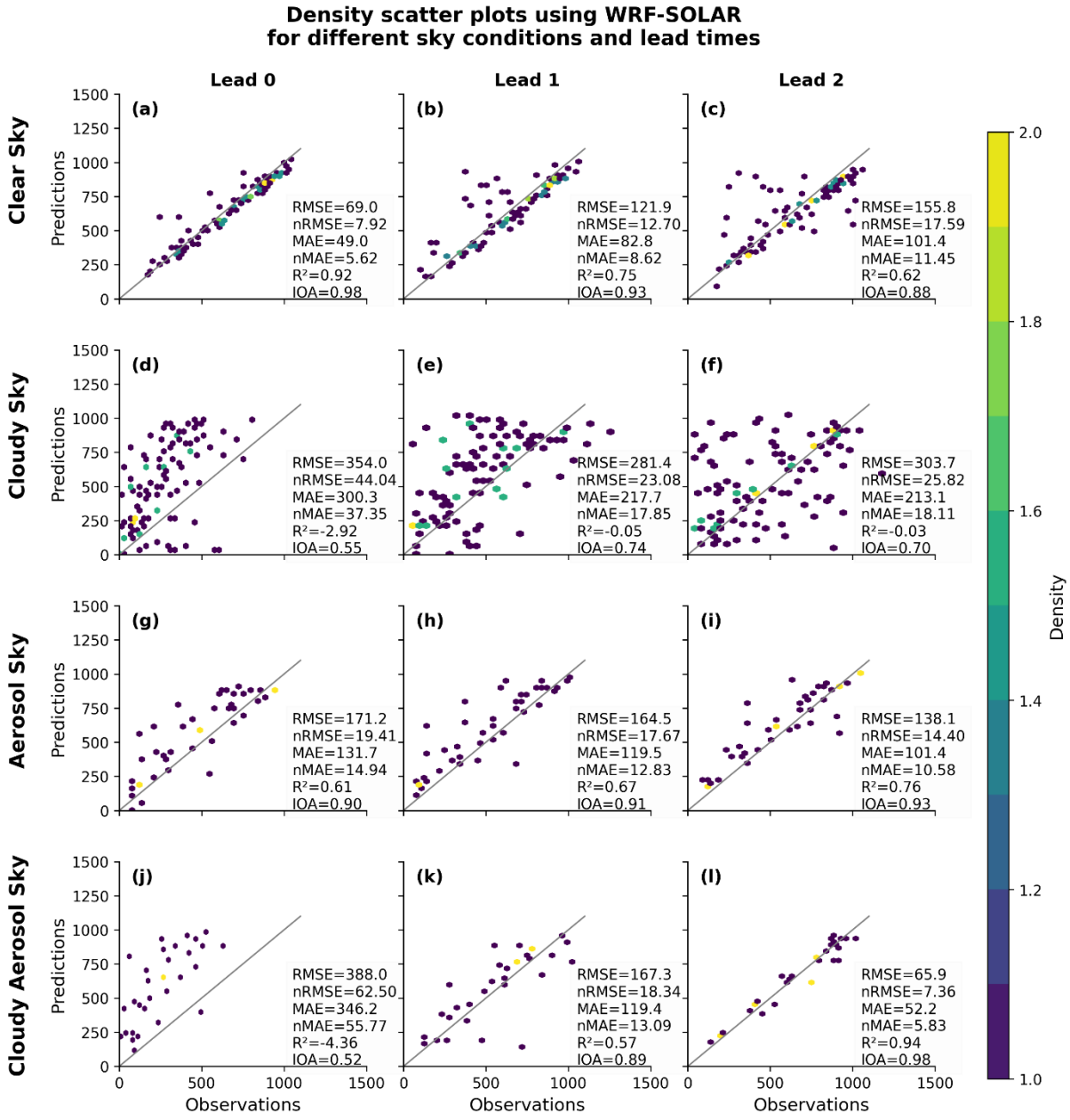

Figure 10: Evaluation of WRF-Solar simulations of hourly forecasted GHI density against observational data under various leads for the year 2020. The columns depict the forecast lead time. Each of the row represents a weather sky condition with its respective name given on the left side of the figure. RMSE, MAE, R^2, and IOA are root- mean-square error, mean absolute error, coefficient of determination and index of agreement, respectively. The terms nRMSE and nMAE indicate the normalized RMSE and MAE, respectively.

3.2.2 Diurnal cycle

a. Clear sky days

The Figure 11 presents the GHI over time for 10 clear-sky days in 2020. The WRF-Solar model closely follows the observed GHI across all forecast lead times, demonstrating strong

performance under clear-sky conditions. The model accurately captures the expected bell-shaped daily solar curve, with peak irradiance occurring around noon (12:00–13:00).

Lead 0 (Figure 11) aligns most closely with the observed data, confirming the model's high reliability for short-term predictions. Lead 1 (Figure 11) and Lead 2 (Figure 11) also show good agreement, although small deviations from observations become more noticeable, particularly around peak sunlight hours. This is consistent with findings in the literature that forecast accuracy tends to decrease as lead time increases (P. Jimenez et al., 2016; Sawadogo et al., 2024; Huang et al., 2024).

For most days such as January 11, October 12, November 11, and December 13 the predictions match the observations very well. However, a few exceptions are observed. On April 6 and June 29, for example, Lead 2 (Figure 11) slightly overestimates GHI during the morning hours and underestimates it near the peak. These discrepancies may be due to errors in the model's initial conditions, spin-up limitations, or the presence of aerosols or thin clouds not fully accounted for. The peak GHI values range from 800 to 1000 W/m², which is typical for clear-sky conditions in tropical or subtropical regions. Overall, the model shows no significant bias in estimating peak values, indicating effective performance of its radiative transfer scheme. The WRF-Solar model is highly reliable for forecasting GHI under clear-sky conditions, even up to 48 hours in advance (Lead 2 (Figure 11)). While a few days show minor discrepancies, these do not significantly affect the model's overall accuracy. Instead, they emphasize the importance of precise input data such as aerosol levels and surface reflectivity, as well as proper model calibration. These findings are in line with previous studies, like those by Jimenez et al. (2016) and Lara-Fanego et al. (2012), which also concluded that WRF-Solar performs best when there is minimal interference from clouds and aerosols.

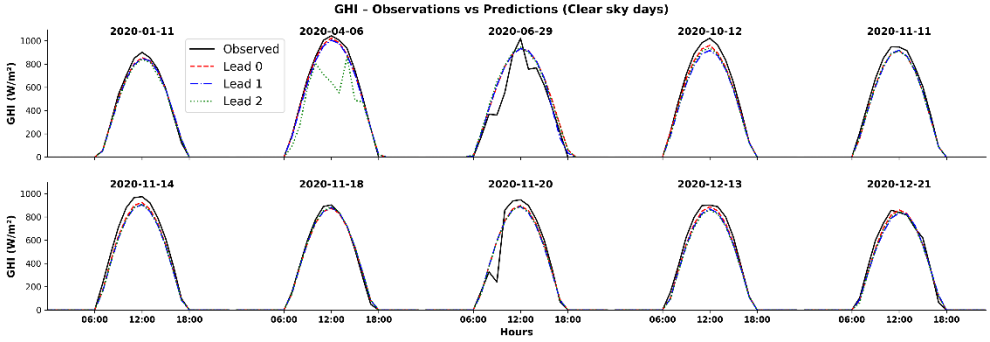

Figure 11: Diurnal cycle of GHI under clear sky days with different leads time.

b. Cloudy sky days

This Figure 12 illustrates the comparison between observed and predicted Global Horizontal Irradiance (GHI) for 10 different cloudy-sky days in 2020. It includes forecasts for Lead 0, Lead 1, and Lead 2.

Unlike clear-sky days, the WRF-Solar model shows noticeable deviations from observed GHI values on cloudy days. The model tends to overestimate irradiance, particularly around midday, when cloud cover often reduces solar radiation in reality but is not fully captured in the model forecast. While observed GHI shows irregular, often flattened or jagged curves due to cloud dynamics, the model continues to predict smooth, bell-shaped profiles, reflecting its tendency to underestimate cloud impacts. Forecast accuracy generally decreases with longer lead times. Lead 0 (Figure 12) (red dashed) is often closest to the observations, while Lead 1 (Figure 12) and especially Lead 2 (Figure 12) show larger errors. For instance, on August 27 and August 25, Lead 2 (Figure 12) significantly overestimates the actual GHI throughout the day. Some days (June 9 and September 5) show that WRF-Solar misses key cloudy periods entirely, predicting high GHI during times of observed irradiance drops highlighting challenges in forecasting cloud timing, development, and movement. Despite the cloud interference, there are cases (March 24 or July 19) where the model still tracks the general trend, suggesting that WRF-Solar retains some predictive power under partially cloudy conditions, especially in short-term forecasts. Thus, WRF-Solar struggles more under cloudy skies, primarily due to uncertainties in cloud representation and the complexity of atmospheric dynamics associated with clouds (variability in cloud thickness, type, and movement).

The model's tendency to produce smooth curves underestimates the variability and intermittency of solar irradiance on cloudy days. The results are consistent with findings in the literature Jimenez et al. (2016) that the model performs best under stable atmospheric conditions and loses accuracy when clouds become the dominant modulating factor. These insights suggest a need for better cloud parameterization, integration of real-time satellite cloud data, or hybrid modelling approaches (combining WRF with ML-based cloud correction techniques) to improve forecast accuracy under such conditions.

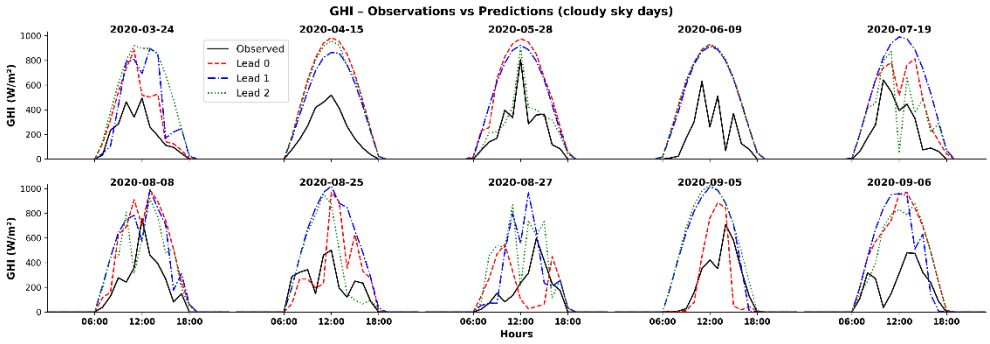

Figure 12: Diurnal cycle of GHI under cloudy sky days with different leads time

c. High aerosol sky days

This Figure 13 compares observed and predicted Global Horizontal Irradiance (GHI) for four aerosol-affected days in March and April 2020. It includes Lead 0, Lead 1, and Lead 2 forecasts from the WRF-Solar model.

Across all four days, the WRF-Solar model captures the general bell-shaped curve of the daily irradiance cycle. This suggests that the model handles the basic solar geometry and atmospheric dynamics well, even in the presence of aerosols.

On aerosol-heavy days like March 4 and April 20, the model tends to overpredict the midday irradiance, especially in Lead 1 and Lead 2. This is a common issue when aerosols are not accurately represented or underestimated in the model initialization (Jimenez et al., 2016; Lara-Fanego et al., 2012).

As expected, forecast accuracy declines from Lead 0 to Lead 2, particularly visible on April 19 and 21, where Lead 2 notably diverges from the observed values. This aligns with literature (Jimenez et al., 2016), which notes that aerosol forecasting is highly sensitive to lead time due to their spatial and temporal variability.

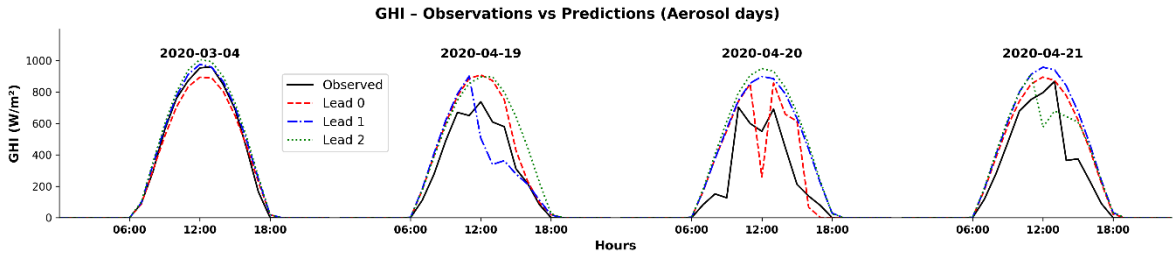

Figure 13: Diurnal cycle of GHI under high aerosol sky days with different leads time

Days like April 20 and 21 show significant dips and flattening in the observed GHI curves around solar noon, likely due to dense aerosol plumes. These dips are not captured by the model, which continues to produce smooth curves, confirming a gap in aerosol-radiation interaction modelling.

The WRF-Solar model maintains reasonable performance under aerosol-heavy skies but with notable limitations in capturing the magnitude and timing of irradiance dips caused by aerosol layers. Improvements in aerosol parameterization and data assimilation are essential to enhance forecasting skill in such conditions particularly for solar energy applications in regions prone to dust, pollution, or biomass burning.

d. Cloudy mixed to high aerosol sky days.

This Figure 14 compares WRF-Solar forecasted Global Horizontal Irradiance (GHI) against observed values for three complex days March 24, April 15, and June 9, 2020 characterized by the combined presence of clouds and high aerosol loads.

All three days show a large mismatch between the observed GHI (black line) and the model outputs (coloured dashed lines), especially during midday. This clearly illustrates the challenge of accurately forecasting irradiance under mixed atmospheric conditions (clouds + aerosols).

The WRF-Solar model consistently overestimates GHI for all lead times, particularly around solar noon. This is most evident on April 15 and June 9, where Lead 0, Lead 1, and Lead 2 predict smooth, high bell-shaped curves, while the observed irradiance is lower and more erratic.

The observed GHI curves are flattened and irregular, likely due to rapidly changing cloud cover and varying aerosol optical depths (AOD). The model's inability to capture these short-term, localized variations leads to pronounced errors.

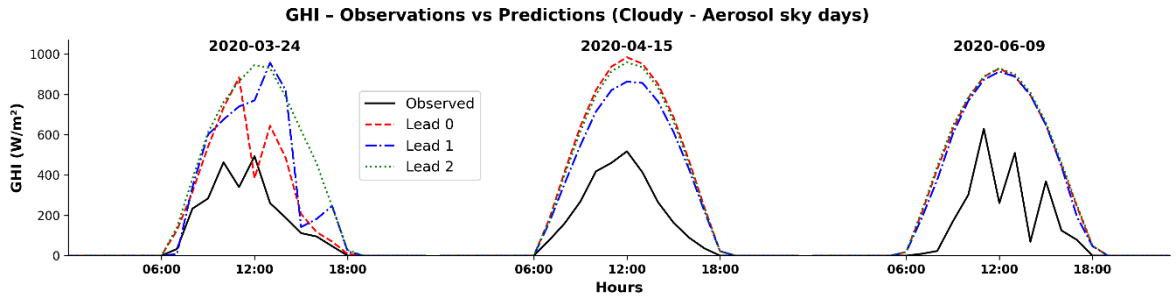

Figure 14: Diurnal cycle of GHI under cloudy mixed to high aerosol sky days with different leads time.

Despite inaccuracies, the WRF-Solar forecasts retain consistent timing of the GHI peaks, suggesting that the model's solar position and basic atmospheric dynamics are correct. The main limitation lies in its inability to represent the cloud-aerosol interaction effects on radiation (Cheng et al., 2022).

Overall, this Figure 14 underscores the limited capability of WRF-Solar to predict solar irradiance under complex sky conditions, where both cloud dynamics and aerosol effects are simultaneously active. While the model performs well under clear skies or even moderate aerosol loads, its radiative transfer and cloud-aerosol parameterizations require enhancement to handle cloud-aerosol coupling and variability.

3.3 Machine Learning Models Performance Against Observations

3.3.1 Scatter plot

To assess the predictive performance of the three ML models: Random Forest (RF), and Support Vector Regression (SVR), Long Short-Term Memory (LSTM) density scatter plots were generated under four distinct sky conditions: Clear Sky, Cloudy Sky, Aerosol Sky, and Cloudy-Aerosol Sky. Each model was evaluated across three lead times: Lead 0**,** Lead 1**,** and Lead 2. Performance metrics such as Root Mean Square Error (RMSE), Mean Absolute Error (MAE), normalized versions of these errors, the coefficient of determination (R^2), and the Index of Agreement (IOA) were computed and annotated in Figure 15, Figure 16, and Figure 17.

Figure 15 presents density scatter plots comparing the predicted and observed Global Horizontal Irradiance (GHI) using a Machine Learning Random Forest (ML-RF) model.

Under clear sky conditions, the RF performs best, particularly at Lead 0 (Figure 15 (a)), where the RMSE is 96.2 W/m², R^2 is 0.21, and the density of points clusters more closely around the

diagonal. However, performance degrades as lead time increases. By Lead 2 (Figure 15 (c)), R^2 drops to 0.18, and errors increase slightly, indicating diminished predictive accuracy with time.

In cloudy conditions, RF performance is much poorer. At Lead 0, for example (Figure 15 (d)), $R^2 = -0.64$, and model outcomes are quite far from observations. Errors are also much larger, with RMSE = 230.3 W/m² and MAE = 187.1 W/m². This poor performance continues through Lead 1 and Lead 2, reflecting the inherent difficulty of modelling highly variable cloudy periods.

Aerosol-affected days shows moderately improved performance compared to cloudy skies. The model achieves its best fit in (Figure 15 (i)) at Lead 2, where R^2 reaches 0.51 and RMSE is reduced to 91.9 W/m². The predictions under aerosol influence alone appear to be more reliable than under cloudy or mixed conditions.

The worst overall performance reveals under cloudy aerosol sky. At Lead 0 (Figure 15 (j)), the model yields an RMSE of 290.7 W/m² and a dramatically negative R^2 of -1.91, indicating a strong mismatch between predicted and observed values. Although performance improves somewhat by Lead 2 (Figure 15 (l)), with R^2 rising to 0.49, the errors remain relatively high.

Overall, the model predicts GHI most accurately under clear skies, with performance decreasing progressively as weather conditions become more complex (with the presence of clouds and aerosols) and as the forecast lead time increases. The results highlight the model's limitations in capturing rapid and uncertain variations in solar irradiance, especially under mixed or overcast conditions.

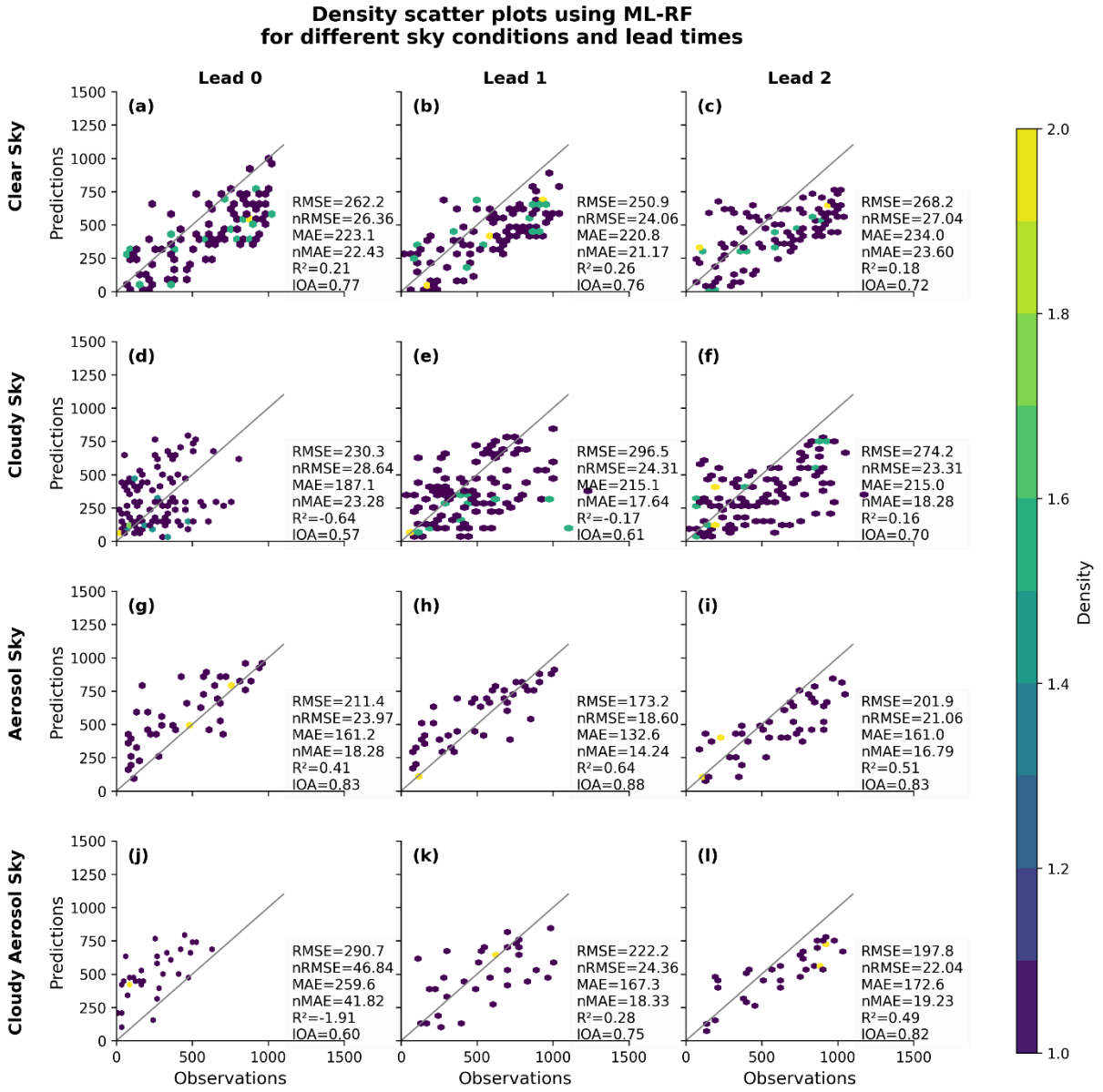

Figure 15: All-sky evaluation of RF model simulations of hourly forecasted GHI density versus observational data with a density between 1 and 2 for the year 2020.

The Figure 16 presents density scatter plots comparing predicted versus observed GHI using a Support Vector Regression (SVR) model under four sky conditions (Clear, Cloudy, Aerosol, and Cloudy-Aerosol) across three lead times: Lead 0, Lead 1, and Lead 2.

- **Clear Sky**: Predictions align reasonably well with observations ($R^2 \approx 0.35$), though performance slightly decreases with lead time. RMSE increases from 203.97 to 257.3, and Index of Agreement (IOA) drops from 0.83 to 0.78.
- **Cloudy Sky**: The model performs poorly (R^2 as low as -0.09), especially as lead time increases, indicating difficulty in capturing GHI under high cloud variability.

- **Aerosol Sky**: Moderate accuracy is observed, with the best performance at Lead 1 (R^2 = 0.64, IOA = 0.90), suggesting that aerosol-affected conditions may be better captured with short lead predictions.
- **Cloudy-Aerosol Sky**: Mixed results, with good performance at Lead 0 (R^2 = 0.88) but significant decline at Lead 1 (R^2 = 0.17), likely due to increased complexity in atmospheric interactions.

Overall, prediction accuracy decreases with longer lead times and under more variable sky conditions, highlighting the challenges of forecasting solar radiation in complex atmospheres.

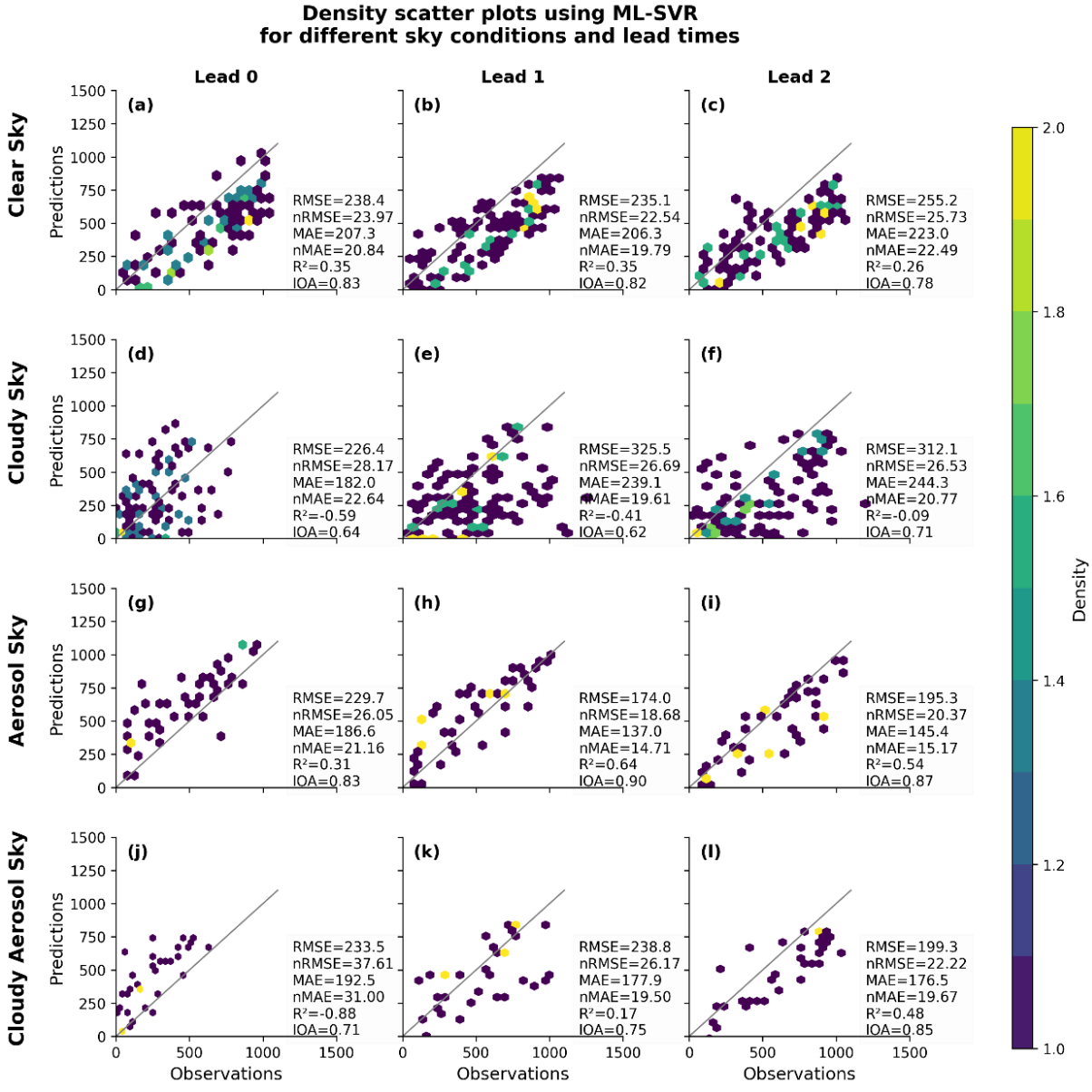

Figure 16: All-sky evaluation of SVR model simulations of hourly forecasted GHI density versus observational data with a density between 1 and 2 for the year 2020.

This Figure 17 shows density scatter plots of predicted vs. observed GHI using an LSTM model under four sky conditions and three lead times (Lead 0 to Lead 2).

- ***Clear Sky***: The LSTM model performs very well across all lead times, with strong correlations (Figure 17) (R^2 from 0.79 to 0.68) and high agreement (IOA > 0.9). Error metrics remain relatively low, showing the LSTM's ability to capture clear sky patterns reliably.
- ***Cloudy Sky***: Accuracy is poor at Lead 0 (Figure 17) (R^2 = –0.09), but improves significantly at longer lead times (R^2 = 0.56 at Lead 2). This may indicate the model adapts better to evolving cloudy conditions with some forecasting horizon.
- ***Aerosol Sky***: Consistently moderate performance ($R^2 \approx 0.55$–0.82), with improved prediction at Lead 2 (Figure 17). The model handles aerosol-related variability reasonably well.
- ***Cloudy-Aerosol Sky***: Initial performance is very poor at Lead 0 (Figure 17) (R^2 = –3.21), but improves considerably by Lead 2 (Figure 17) (R^2 = 0.82), showing that the model can gradually learn complex interactions with longer forecasting windows.

In short, the LSTM model demonstrates strong performance under clear conditions and shows adaptability with longer lead times in complex skies, particularly under aerosol and mixed cloud-aerosol influence.

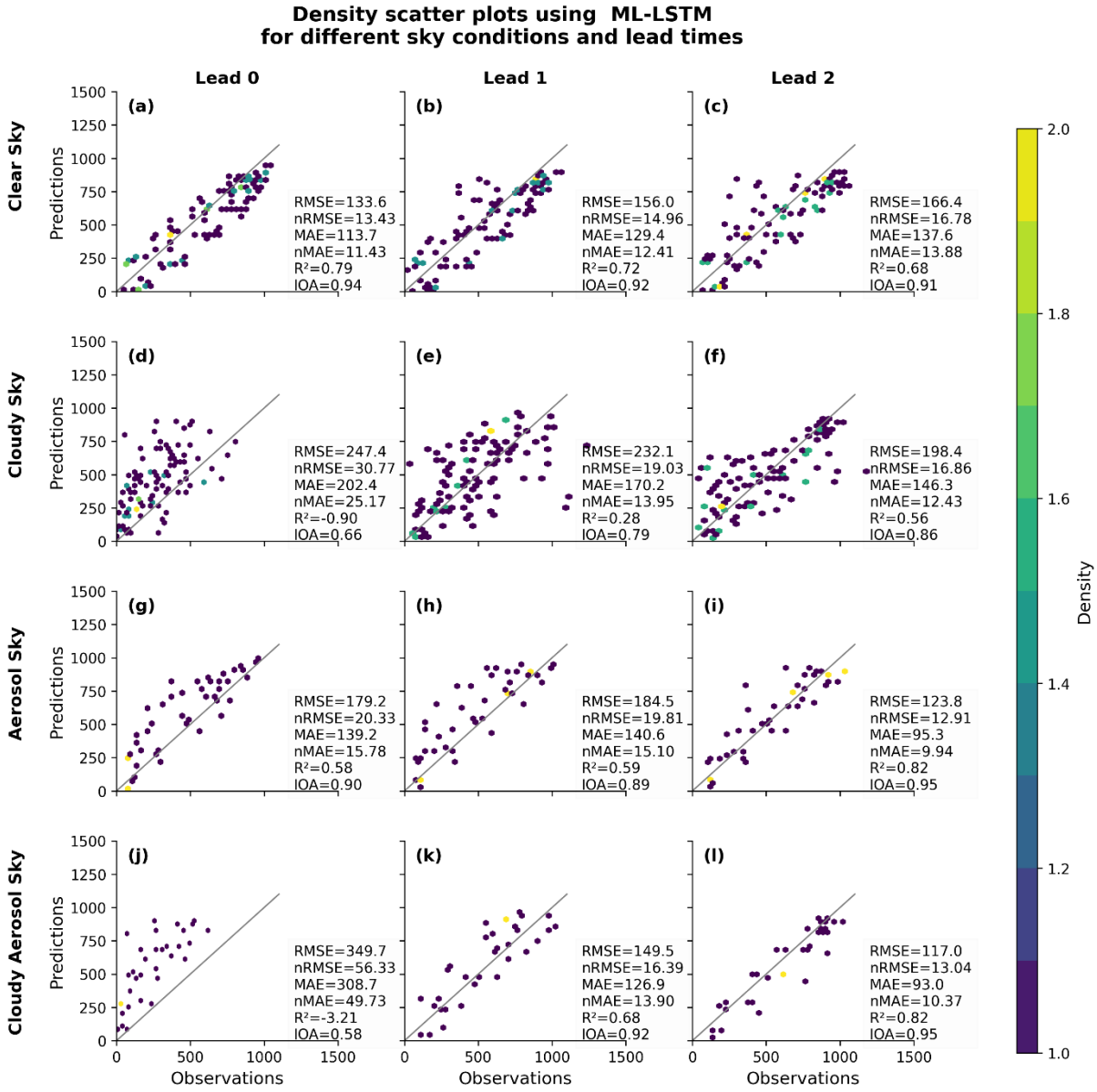

Figure 17: All-sky evaluation of LSTM model simulations of hourly forecasted GHI density versus observational data with a density between 1 and 2 for the year 2020.

3.3.2 Diurnal cycle for ML models:

a. ML-RF Model

Figure 18 illustrates the diurnal GHI cycle for ten clear-sky days in 2020, comparing observed data with Random Forest (RF) model predictions at lead times of Lead 0, Lead 1, and Lead 2. The RF model captures the general bell-shaped profile of solar irradiance, particularly at Lead 0 (Figure 18). However, the prediction accuracy deteriorates as the lead time increases, with underestimations near solar noon becoming more frequent. This pattern is consistent with findings by Voyant et al. (2017b) and Lorenz et al. (2009), who reported the limited capability of non-sequential ML models to preserve temporal dynamics in solar forecasting. Seasonal

variation is also evident, with lower GHI values in December attributed to reduced solar elevation and shorter day lengths, in line with standard solar radiation theory (Duffie, J. A., & Beckman, 2013).

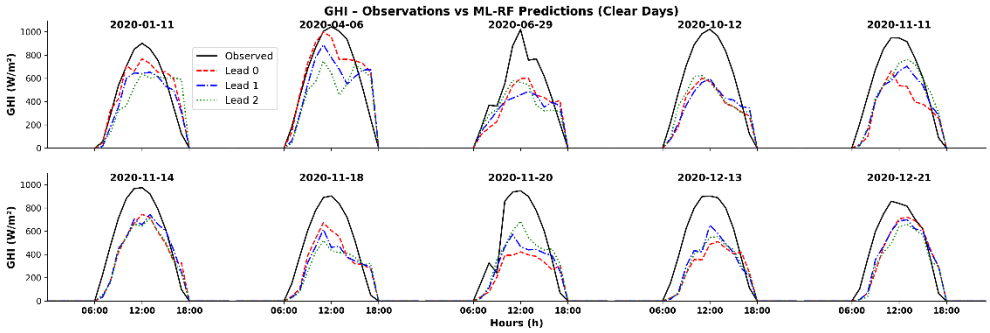

Figure 18: Diurnal GHI cycle for ten clear-sky days in 2020 using RF model.

The diurnal cycle of GHI predicted by the ML-RF model was compared against observations across several cloudy days (Figure 19). The model generally reproduces the daily solar cycle shape, with peak irradiance around solar noon, consistent with prior findings on machine learning models' ability to capture solar geometry (Lara-Fanego et al., 2012b). However, discrepancies increase under cloudy conditions, particularly with higher lead times, where the model frequently overestimates GHI due to limited representation of dynamic cloud cover (Lorenz et al., 2009; Chu et al., 2013). The rapid variability in observed GHI, characteristic of broken clouds, poses a known challenge for ML models (D. Yang et al., 2018; Marquez & Coimbra, 2013). Forecast skill deterioration with longer lead times also aligns with the literature, as forecast uncertainty compounds over time (M. Li et al., 2021). In summary, the ML-RF model performs best at Lead 0, benefiting from more recent input data, while performance decreases at Lead 1 and Lead 2 due to increasing uncertainty in cloud evolution.

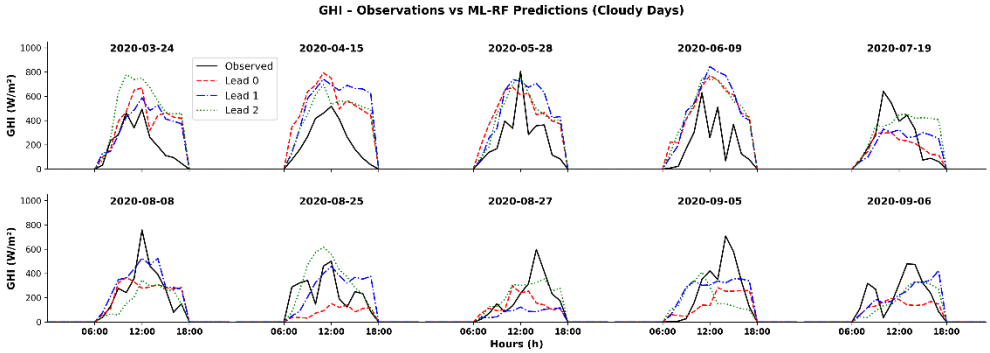

Figure 19: Diurnal GHI cycle for ten cloudy-sky days in 2020 using RF model.

The diurnal GHI patterns simulated by the ML-RF model for aerosol-affected days exhibit notable overestimation during peak solar hours (Figure 20). While the model captures the

general daily cycle well, it systematically underestimates the attenuation caused by aerosols, particularly for longer lead times. This behaviour is consistent with previous findings that highlight the significant radiative impact of aerosols through both scattering and absorption mechanisms (Charlson et al., 1992; IPCC, 2013). The model's performance degradation with increasing lead time mirrors the general trend reported by Marquez and Coimbra (2013) and D. Yang et al. (2018), where forecast uncertainty grows with the forecast horizon. The RF algorithm's limited performance under aerosol-heavy conditions reflects its dependency on accurate input features, and the lack of real-time aerosol data likely contributes to the observed errors (Chu et al., 2016). Incorporating real-time (AOD) measurements or satellite-derived aerosol indices could enhance model skill, as proposed by Luo et al. (2024) and Kumi et al. (2009).

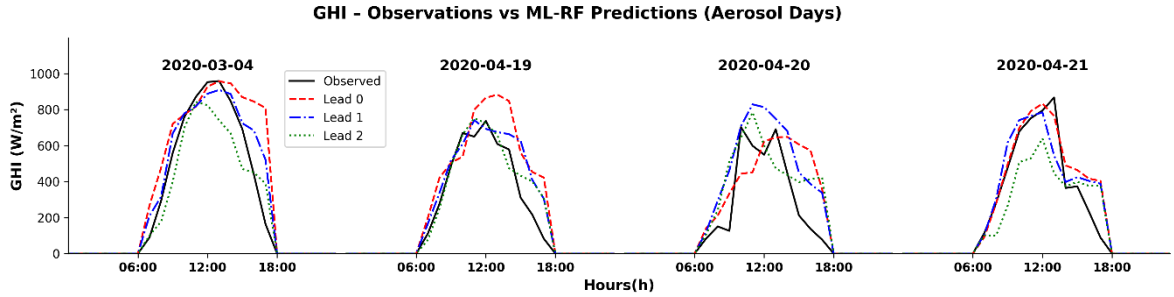

Figure 20: Diurnal GHI cycle for four aerosol affected sky days in 2020 using RF model

The Figure 21 illustrates the performance of a Random Forest (RF) model in predicting GHI for three specific days classified as cloudy-aerosol conditions: March 24, April 15, and June 9 of 2020. The plots compare observed GHI values (solid black lines) with predictions from the RF model at three lead times: Lead 0, Lead 1, Lead 2.

Across all three days, the observed GHI curves show significant variability and dips, which are typical under cloudy-aerosol conditions due to fluctuating solar radiation reaching the surface.

The Lead 0 predictions closely follow the observed patterns, especially in the timing of the irradiance peaks. However, they tend to overestimate the GHI values during peak hours.

Lead 1 and Lead 2 predictions also capture the general diurnal trend but tend to smooth out the short-term fluctuations present in the observed data, likely due to the compounding uncertainty over time.

On June 9, 2020, the RF model performed notably well, with all lead times showing relatively good alignment with the observed curve, indicating better predictability under those specific atmospheric conditions.

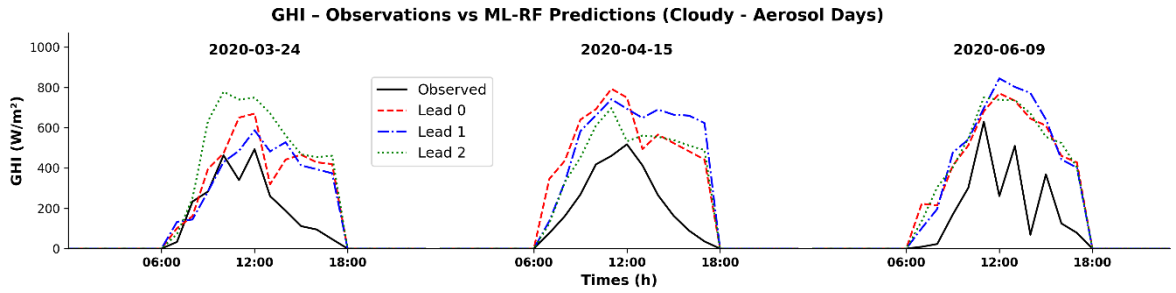

Figure 21: Diurnal GHI cycle for three aerosol affected sky days in 2020 using RF model

The RF model demonstrates reasonable predictive skill under complex atmospheric conditions involving both clouds and aerosols. While the accuracy decreases slightly with increasing lead time, the model maintains the overall shape and trend of the GHI curve. These results suggest that the Random Forest approach, even without sequential modelling, can offer valuable short-term GHI forecasts useful for solar energy applications, though its limitations in capturing rapid fluctuations under variable sky conditions must be acknowledged.

b. ML-SVR model

Figure 22, Figure 23, Figure 24, Figure 25 present the comparison between observed GHI and predictions from the ML-SVR model over four distinct sky conditions: clear, cloudy, aerosol-affected, cloudy-aerosol days. Each plot represents hourly GHI values for a specific day, with forecast horizons.

The Figure 22 (Clear Days) displays model predictions under stable, low-aerosol, cloud-free conditions:

Predictions during clear days show consistent underestimation of peak GHI, especially for Lead 2, which may be due to the model being conservative in the absence of atmospheric disturbances.

The diurnal shape is well preserved in almost all cases, indicating that the model learned the temporal solar cycle effectively.

On days like 2020-11-14 and 2020-12-21, all leads follow the observed curve well, confirming the predictability of GHI in stable atmospheric conditions.

Some days, like 2020-04-06 and 2020-06-29, show a sharper drop-off in model accuracy, possibly due to subtle changes in transparency (thin clouds or haze).

Overall, the ML-SVR performs best on clear-sky days, with smooth and accurate diurnal shapes, especially for Lead 0 and Lead 1.

The Figure 23 (Cloudy Days) highlights model performance under cloud-dominated conditions:

Predictions are less accurate and more variable, reflecting the high temporal and spatial variability of clouds. The model tends to smooth out sharp variations in observed GHI (2020-06-09, 2020-08-08), indicating difficulty in capturing fast-changing cloud cover.

On several days (2020-09-06), none of the leads match the observed curve well, especially around peak hours, showing significant uncertainty even at Lead 0.

In some instances (2020-05-28, 2020-08-25), Lead 2 surprisingly performs comparably to Lead 0, possibly due to reliance on smoothed input features.

The Figure 24 (Aerosol Days) illustrates the ML-SVR model's performance during high aerosol loading conditions.

The SVR shows a relatively good ability to capture the overall diurnal pattern, particularly for Lead 0, although it tends to overestimate peak GHI (2020-03-04).

For Lead 1 and Lead 2, the performance degrades slightly, with underestimations in the afternoon (2020-04-19) and discrepancies in curve shapes (2020-04-20).

On 2020-04-21, Lead 0 follows observed values closely, while Lead 2 fails to replicate the peak GHI, showing the increasing uncertainty with forecast horizon.

These patterns reflect the challenging nature of aerosol interference, which can vary rapidly and is often difficult to model accurately beyond the current day.

The evaluation performance of a SVR model in GHI during cloudy-aerosol days (Figure 25), specifically on March 24, April 15, and June 9, 2020.

- *On March 24*, the observed GHI shows multiple fluctuations, likely due to intermittent cloud coverage. While Lead 0 predictions partially follow the trend, Lead 1 (Figure 25) and Lead 2 (Figure 25) increasingly overestimate GHI, especially during midday.
- *On April 15*, the SVR model effectively captures the diurnal curve shape. However, all lead-time predictions overestimate the observed GHI, indicating the model's limited responsiveness to irradiance reduction caused by clouds and aerosols.
- On June 9, the observed GHI again shows rapid variability. The SVR model produces smooth predictions that do not reflect short-term drops in irradiance, though the general shape and timing of the curve are maintained.

Globally, the SVR model shows competence in capturing the general GHI trend under cloudy-aerosol conditions, but tends to overpredict irradiance, particularly at higher lead times. Its relatively smooth output suggests that while SVR is effective for modelling overall diurnal solar patterns, it may lack the adaptability to respond to rapid, short-duration fluctuations caused by dynamic cloud-aerosol interactions. As a result, SVR may be better suited for coarse forecasting

or average trend estimation**,** rather than detailed intra-day solar variability under complex sky conditions. This behaviour confirms that clouds pose the greatest challenge for short-term GHI forecasting, even with advanced ML models like SVR.

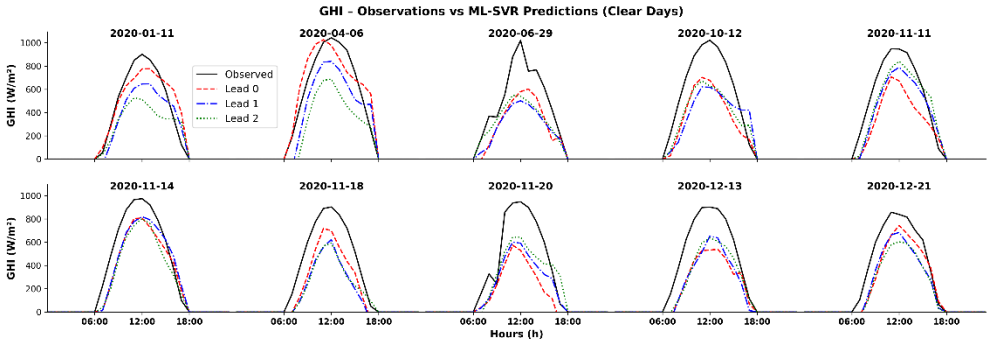

Figure 22:Diurnal GHI cycle for ten clear sky days in 2020 using SVR model

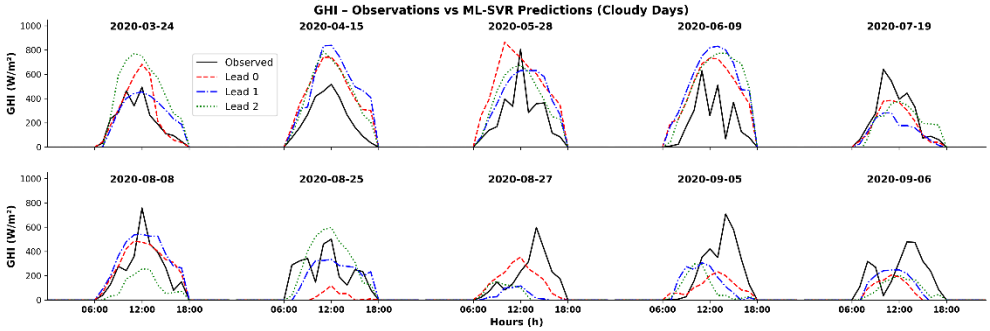

Figure 23:Diurnal GHI cycle for ten cloudy sky days in 2020 using SVR model

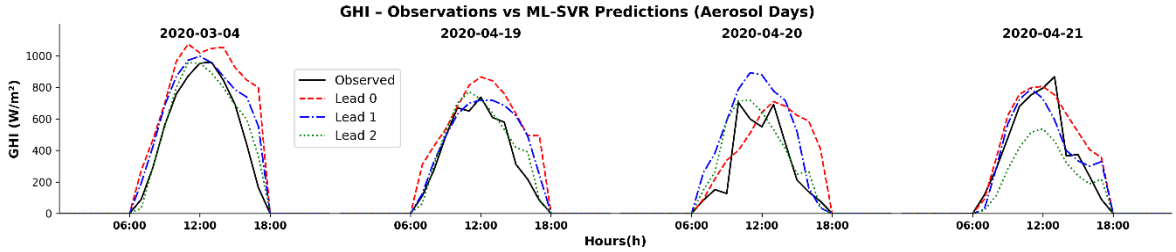

Figure 24:Diurnal GHI cycle for four aerosol sky days in 2020 using SVR model

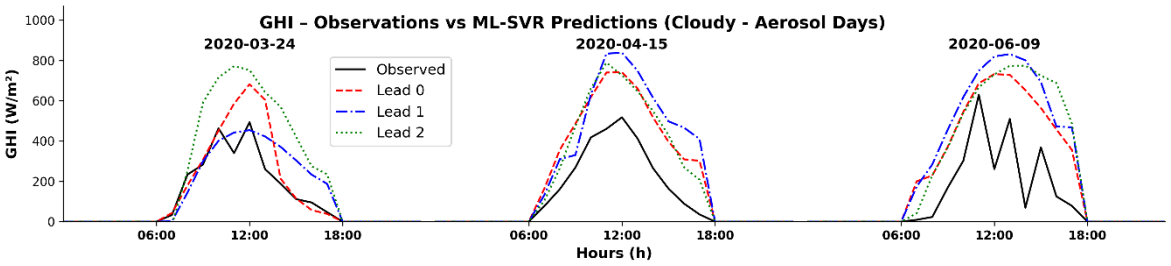

Figure 25: Diurnal GHI cycle for three cloudy-aerosol sky days in 2020 using SVR model

c. ML-LSTM model.

On clear days (Figure 26), the diurnal pattern of GHI follows a smooth bell shape, and the ML-LSTM model reproduces this behaviour remarkably well. The model predictions closely track the observed peaks and slopes, with minimal lag or amplitude error across all forecast leads. These results align with Gallo et al. (2022), who highlighted that deep learning models perform best under stable and clear atmospheric conditions due to the regularity of solar patterns. The errors across Lead 0 to Lead 2 are almost indistinguishable, demonstrating the model's robustness in short-term forecasting under ideal conditions.

Under cloudy conditions in the Figure 27, observed GHI becomes highly variable with frequent dips and spikes due to intermittent cloud coverage. The ML-LSTM model, while still capturing the general diurnal structure, tends to overpredict GHI throughout the day. The forecasts show smoother curves compared to the observed jagged profiles, indicating a limitation in representing rapid transients caused by broken clouds. This is consistent with (Naveed et al., 2025), who noted that temporal granularity and the lack of high-frequency satellite data hinder prediction precision under unstable sky conditions.

Interestingly, the prediction accuracy decreases slightly from Lead 0 to Lead 2, reflecting the increasing uncertainty with longer forecast horizons. However, the model still maintains the overall energy trend, which is valuable for power system planning where averaged GHI values are often sufficient.

In the Figure 28, during aerosol-rich days, the observed GHI exhibits notable attenuation, particularly near midday peaks. The ML-LSTM model tends to overestimate GHI in these conditions, especially for Lead 0. This is consistent with findings by Alkhayat et al., (2024), where models trained primarily on meteorological data often struggle to fully account for rapid and heterogeneous aerosol effects without high-resolution aerosol profiles. The inclusion of AOD (aod550) as an input improved the trend capture, but some temporal shifts in peak intensity were still noted, especially for Lead 1 and Lead 2.

The Figure 29 presents the performance of a LSTM model in predicting Global Horizontal Irradiance (GHI) on days dominated by aerosol atmospheric conditions mixed to cloudy sky**:** March 24, April 15, June 09. On each date, the observed GHI (black curve) shows irregular and dampened patterns characteristic of cloud and aerosol interference, particularly during midday when GHI typically peaks. In contrast, all LSTM predictions (coloured dashed lines) display smooth, bell-shaped diurnal profiles, resembling ideal clear-sky patterns. This discrepancy suggests that the LSTM model, while capturing the overall daily cycle, tends to overestimate solar irradiance under disturbed atmospheric conditions due to its limited ability to model abrupt, high-frequency fluctuations caused by transient clouds or aerosols.

The LSTM model demonstrates excellent forecasting ability for GHI under aerosol-dominated conditions. Its capacity to learn and reproduce temporal patterns is evident in the consistent match across different lead times. The model's performance, especially for short to medium-range forecasts, suggests its suitability for solar resource prediction, particularly in relatively stable atmospheric scenarios where aerosols dominate over clouds. However, minor overestimations at the peak may indicate the model's inability to fully capture transient attenuation events, such as sudden changes in aerosol optical depth.

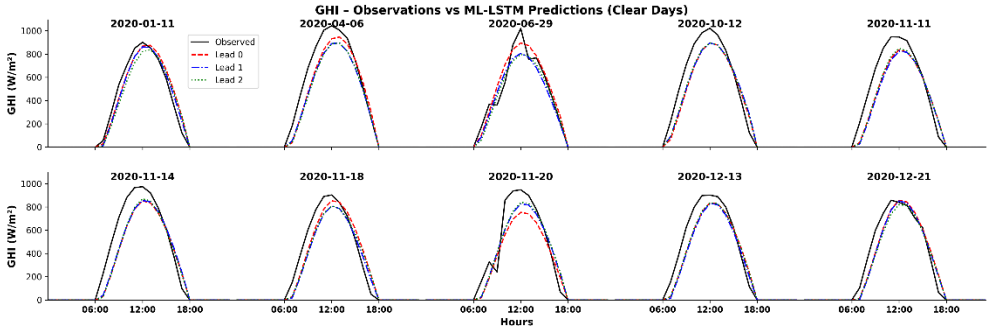

Figure 26: Diurnal GHI cycle for clear sky days in 2020 using LSTM model

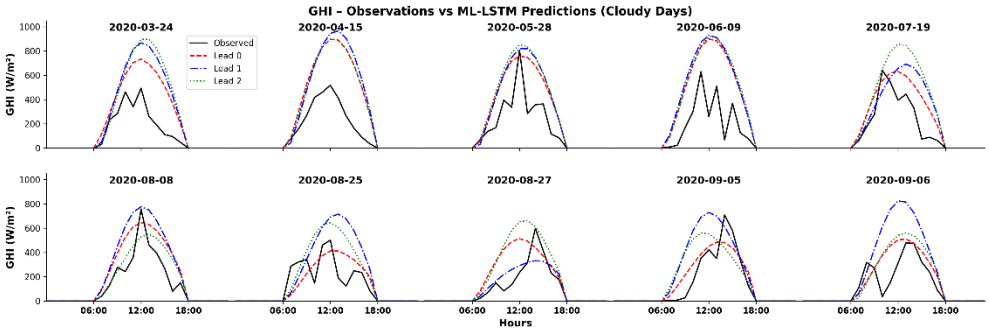

Figure 27: Diurnal GHI cycle for cloudy sky days in 2020 using LSTM model

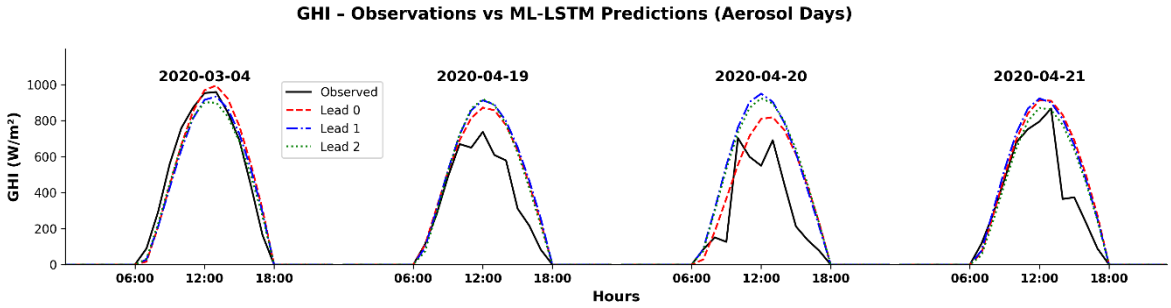

Figure 28: Diurnal GHI cycle for aerosol sky days in 2020 using LSTM model

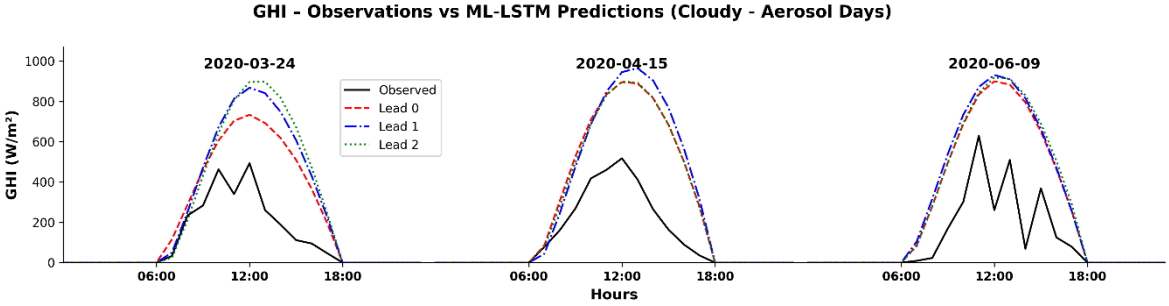

Figure 29: Diurnal GHI cycle for cloudy-aerosol sky days in 2020 using LSTM model

3.4 Comparative Analysis: WRF-Solar vs. Machine Learning Models

In order to provide more insights in the comparison of WRF-Solar model to the three ML models chosen. we present the Figure 30 which illustrates the skill scores of various models (WRF-Solar, LSTM, RF, and SVR) compared to the Persistence model across different sky conditions (clear, cloudy, aerosol, cloudy mixed to aerosol) and lead times.

The Persistence model serves as the reference baseline (Skill Score = 0), with positive values indicating improved performance relative to the reference and negative values indicating poorer performance.

The skill score metric indicates how much better or worse each model performs relative to the Persistence model.

- The WRF-Solar model generally outperforms the Persistence benchmark across most sky conditions particularly under clear, cloudy, and cloudy-aerosol scenarios as shown by its positive skill scores at shorter lead times. However, under aerosol-dominated skies, its performance drops below the reference. While WRF-Solar's skill scores tend to decline slightly as lead time increases, the model remains competitive and more robust than most ML models under less complex atmospheric conditions.
- Machine Learning Models (LSTM, RF, SVR) exhibit mixed performance. While LSTM tends to outperform the Persistence model under certain cloudy and mixed conditions**,** ML models overall show varying skill scores depending on sky condition and lead time. Under clear and aerosol-dominated skies, some ML models (notably RF and SVR) perform worse than the Persistence benchmark, as reflected by their negative skill scores.

Under clear skies, WRF-Solar and some ML models (LSTM) show strong performance, likely due to the predictability of solar irradiance in stable conditions. RF and SVR may lag behind, suggesting limited adaptability to even simple scenarios.

Under clear conditions, WRF-Solar consistently outperforms all machine learning models, especially at lead time Lead 0 (Figure 30), where it achieves a notably high skill score (~0.6). In contrast, all ML models, particularly RF and SVR, show significantly negative scores, indicating poorer performance than the Persistence model. This highlights WRF-Solar's superior capacity to model deterministic and physically-driven patterns typical of clear sky radiation.

ML models especially LSTM and SVR surpass WRF-Solar under cloudy conditions, with LSTM achieving the highest skill score at Lead 1 (~0.3). WRF-Solar struggles here, showing slightly negative or neutral performance across lead times. This suggests that ML models are better at capturing complex, nonlinear cloud dynamics where physical models may lack sufficient input resolution or real-time cloud feedback.

In aerosol-laden skies, all models perform worse than the Persistence baseline, with consistently negative skill scores. However, WRF-Solar maintains a slightly better performance than most

ML models, particularly at Lead 2. The poor performance of ML models may be due to the high uncertainty and temporal variability in aerosol properties, which are difficult to capture from limited training data.

Under the mixed cloudy-aerosol scenario, all models achieve their best relative performance, with positive skill scores at Lead 1. Notably, LSTM outperforms WRF-Solar, followed closely by WRF-Solar and RF. This indicates that ML models, especially LSTM, benefit from complex hybrid patterns where data-driven learning can capture interactions between cloud and aerosol effects, surpassing the rule-based approach of WRF-Solar

In summary, all models exhibit a general decline in skill score as lead time increases, which is expected due to the inherent uncertainty in longer-term forecasts. However, WRF-Solar's decline is more gradual compared to the sharper drops observed in some ML models (SVR), indicating better handling of temporal dependencies.

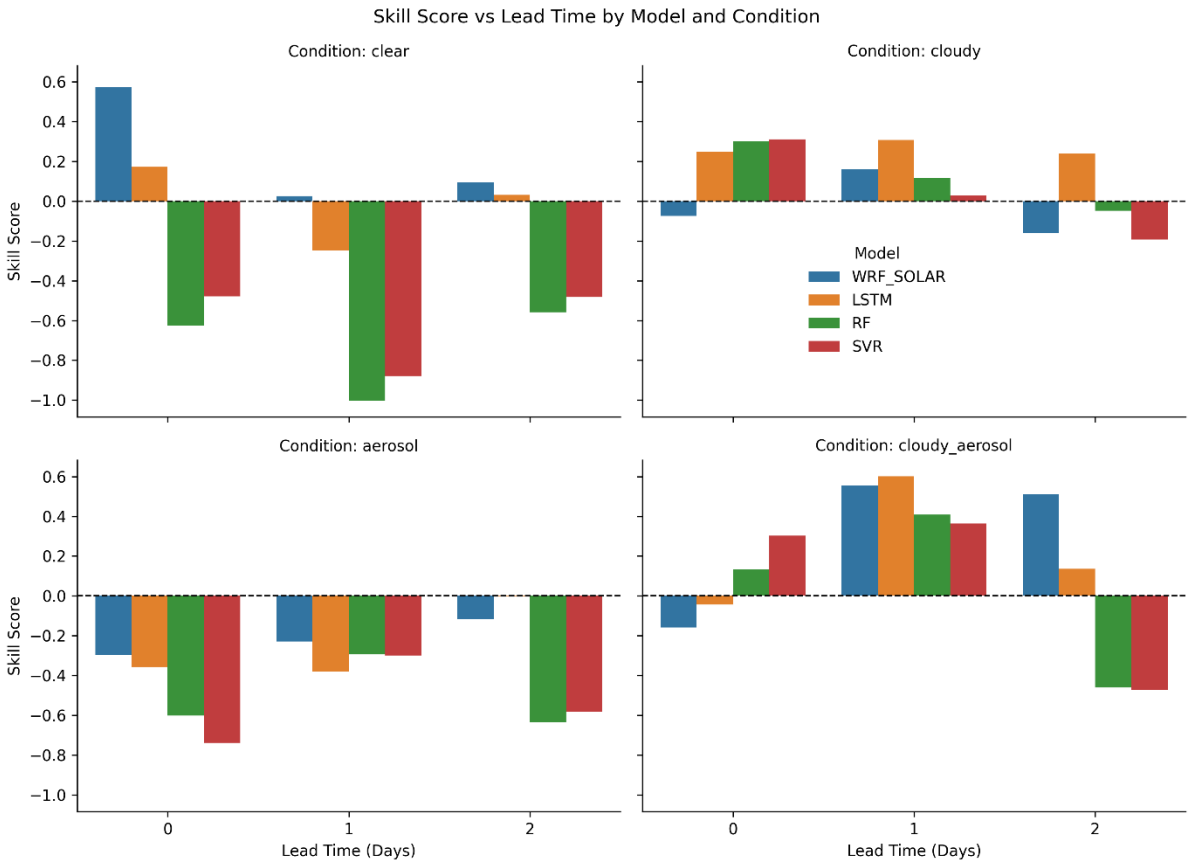

Figure 30: Model comparison under various sky conditions and lead times.

3.5 Discussion

This study aimed to compare the performance of the WRF-Solar model and machine learning (ML) approaches such as Random Forest (RF), Support Vector Regression (SVR), and Long Short-Term Memory (LSTM) for three-day-ahead solar irradiance forecasting under various atmospheric conditions in Burkina Faso. The findings provide clear insights into the strengths and limitations of each forecasting method across different weather scenarios and lead times.

Under clear-sky conditions, the WRF-Solar model performed exceptionally well (Sawadogo et al., 2024), with high skill scores and strong consistency across all lead times. It significantly outperformed the Persistence model and was the most accurate among all tested approaches. Machine Learning models, particularly RF and SVR, showed negative skill scores under these conditions, indicating poor performance relative to the baseline. LSTM showed a slightly positive skill score only at longer lead times but still did not surpass WRF-Solar.

In contrast, cloudy conditions exposed the limitations of WRF-Solar (Mwigereri et al., 2025), with lower skill scores likely due to its difficulty in capturing the rapid dynamics of cloud cover. ML models, especially LSTM and SVR, performed better under these variable conditions, with LSTM achieving the highest skill score at lead time 1. This indicates the superior adaptability of data-driven models under conditions of increased atmospheric uncertainty.

Under aerosol-laden skies, all models performed poorly compared to the Persistence benchmark. WRF-Solar exhibited slightly better but still negative skill scores, while ML models including LSTM, RF, and SVR failed to provide reliable forecasts. This suggests that aerosol variability remains challenging for both physical and data-driven models, likely due to limited or noisy observational inputs.

For cloudy-aerosol mixed conditions, forecasting accuracy declined across the board, yet ML models again outperformed WRF-Solar. LSTM showed relatively higher skill scores, highlighting its ability to learn complex nonlinear interactions between clouds and aerosols(Jiang et al., 2024), which are often not well-represented in numerical weather prediction models like WRF-Solar.

A notable trend across all conditions was the decrease in model performance with increasing lead time, particularly for WRF-Solar. This reflects the known issue of error propagation in physical models over time. In comparison, ML models maintained more stable performance, with LSTM consistently showing better adaptation at longer lead times.

Overall, ML approaches especially LSTM demonstrated greater flexibility and stronger adaptation to local atmospheric variability in Burkina Faso, particularly under complex or

uncertain conditions. However, WRF-Solar remains a robust physical modelling tool, particularly under deterministic conditions like clear skies, and remains valuable for operational forecasting in data-sparse regions or regulatory applications.

Conclusion and Perspectives

Conclusion

This research compared the performance of the WRF-Solar model and three ML techniques such as RF, SVR, and LSTM for short-term solar irradiance forecasting in Burkina Faso over the year 2020. The results show that while WRF-Solar performs well under clear skies, its accuracy significantly drops under cloudier and aerosol-heavy conditions. Thus, the hypothesis 1 is not verified and confirm all results that indicate ML models, particularly LSTM, consistently outperformed WRF-Solar across cloudy and cloudy sky affected by high aerosol, highlighting their potential for operational use in solar energy planning.

On the other hand, under aerosol conditions, both WRF-Solar and ML models perform worse than the persistence model, emphasizing the potential benefit of using a hybrid approach.

Based on hypotheses, the outcomes indicate partial confirmation:

The initial hypothesis is rejected: unexpectedly, WRF-Solar outperformed ML models under clear-sky conditions, confirming its proficiency for stable, predictable scenarios.

The second hypothesis is verified: ML models, and especially LSTM, performed better than WRF-Solar under clouded conditions, where physical models struggle with rapid variability.

Hypothesis three is partially validated: in high aerosol loading conditions, none of the WRF-Solar or ML models outperformed the persistence model, which indicates the difficulty of prediction under the presence of aerosols and to the need for better aerosol representation in both approaches.

The fourth hypothesis is mostly validated: in mixed cloudy and aerosol conditions, ML models, particularly LSTM, delivered prediction accuracy comparable to or superior to WRF-Solar, vouching for their adaptability in addressing complex atmospheric interactions.

Key conclusions include:

ML models are better suited to handle atmospheric variability, especially under complex conditions such as clouds and aerosols.

WRF-Solar remains a reliable model under stable conditions (clear sky) and serves as a valuable reference.

The integration of high-quality input data (like CAMS and ERA5) improves forecasting for both physical and ML approaches.

LSTM emerged as the most accurate model overall, suggesting that deep learning can significantly enhance mid-range solar forecasts.

Given the growing importance of solar energy in Burkina Faso's energy transition, this work contributes valuable insights toward improving forecast accuracy.

Perspectives

The results of the forecasting models have shown that in the short run, WRF-Solar performs better under clear sky conditions, while machine learning models, particularly LSTM, offer better performance under cloudy and mixed atmospheric conditions. In the long run, LSTM maintains more consistent predictive ability across increasing lead times. The current study therefore calls for other research studies in the same field to investigate other combinations of modelling approaches and input data to improve solar irradiance forecasting in Burkina Faso.

Some future studies can focus on hybrid modelling, combining physical models like WRF-Solar with machine learning algorithms to benefit from both physical consistency and data adaptability. Other research can also be oriented toward comparing different sources of satellite and aerosol data, or evaluating the impact of input data resolution on forecast accuracy. The variability in model performance under different atmospheric conditions suggests that many influencing factors are still not fully captured.

Moreover, further research can investigate how solar forecasting models can be integrated into national energy planning systems, especially in the context of renewable energy expansion and electrification efforts. It would also be useful to examine the economic and operational impacts of improved solar forecasts on grid stability and energy resource management.

Additionally, more attention should be given to the willingness and capacity of local stakeholders such as energy providers and meteorological agencies to adopt and operationalize such models. This could later lead to the development of policy briefs aimed at guiding the government in implementing forecasting systems tailored to Burkina Faso's specific energy and climate context.

Finally, future research may explore the education and training needs of technical personnel in charge of weather and energy systems, to ensure long-term sustainability and local ownership of solar forecasting tools.

References

Abid, H., Thakur, J., Khatiwada, D., & Bauner, D. (2021). Energy storage integration with solar PV for increased electricity access: A case study of Burkina Faso. *Energy*, *230*, 120656. https://doi.org/10.1016/j.energy.2021.120656

Adeniyi, M. O. (2016). *Simulating the influence of doubled CO 2 on the water budget over West Africa us-*. *1992*. https://doi.org/10.26491/mhwm/124787

Akhlaque, M., Ahmad, F., & Akhtar, M. (2009). Estimation of global and diffuse solar radiation for Hyderabad, Sindh, Pakistan. *Journal of Basic and Applied Sciences*, *5*.

Alkhayat, G., Hasan, S. H., & Mehmood, R. (2024). *The Effect of Using Aerosol Variables on the Performance of Deep Learning-Based GHI Forecasting Models*. https://doi.org/10.20944/preprints202401.0880.v1

Allal, Z., Noura, H. N., & Chahine, K. (2024). Machine Learning Algorithms for Solar Irradiance Prediction: A Recent Comparative Study. *E-Prime - Advances in Electrical Engineering, Electronics and Energy*, *7*(December 2023), 100453. https://doi.org/10.1016/j.prime.2024.100453

Augustine, C., & Nnabuchi, M. (2009). Correlation of cloudiness index with clearness index for four selected cities in Nigeria. *The Pacific Journal of Science and Technology*, *10*(2), 568–573. http://www.akamaiuniversity.us/PJST10_2_568.pdf

Azoumah, Y., Ramdé, E. W., Tapsoba, G., & Thiam, S. (2010). Siting guidelines for concentrating solar power plants in the Sahel: Case study of Burkina Faso. *Solar Energy*, *84*(8), 1545–1553. https://doi.org/10.1016/j.solener.2010.05.019

Blaga, R., Sabadus, A., Stefu, N., Dughir, C., Paulescu, M., & Badescu, V. (2019). A current perspective on the accuracy of incoming solar energy forecasting. *Progress in Energy and Combustion Science*, *70*, 119–144. https://doi.org/https://doi.org/10.1016/j.pecs.2018.10.003

Breiman, L., Friedman, J., Olshen, R.A., & Stone, C. J. (1984). Classification and Regression Trees (1st ed.). *Chapman and Hall/CRC.*, 368. https://doi.org/https://doi.org/10.1201/9781315139470

Breiman, L. (1996). Bagging predictors. *Machine Learning*, *24*(2), 123–140. https://doi.org/10.1007/BF00058655

Breiman, L. (2001). Random Forests. *Machine Learning*, *45*(1), 5–32. https://doi.org/10.1023/A:1010933404324

Breiman, L. (2002). Wald lecture 1 machine learning. *Machine Learning*, 1–39.

https://www.stat.berkeley.edu/~breiman/wald2002-1.pdf

BSRN. (2021). Baseline Surface Radiation Network. *World Radiation Monitoring Center*. https://bsrn.awi.de/.

Bui, A., Johnson, F., & Wasko, C. (2019). The relationship of atmospheric air temperature and dew point temperature to extreme rainfall. *Environmental Research Letters*, *14*. https://doi.org/10.1088/1748-9326/ab2a26

Camacho, M., Maldonado-Correa, J., Torres-Cabrera, J., Martín-Martínez, S., & Gómez-Lázaro, E. (2025). Short-Medium-Term Solar Irradiance Forecasting with a CEEMDAN-CNN-ATT-LSTM Hybrid Model Using Meteorological Data. *Applied Sciences (Switzerland)*, *15*(3). https://doi.org/10.3390/app15031275

Charlson, R. J., Schwartz, S. E., Hales, J. M., Cess, R. D., Coakley, J. A., Hansen, J. E., & Hofmann, D. J. (1992). Climate Forcing by Anthropogenic Aerosols. *Science*, *255*(5043), 423–430. https://doi.org/10.1126/science.255.5043.423

Cheng, X., Ye, D., Shen, Y., Li, D., & Feng, J. (2022). Studies on the improvement of modelled solar radiation and the attenuation effect of aerosol using the WRF-Solar model with satellite-based AOD data over north China. *Renewable Energy*, *196*, 358–365. https://doi.org/10.1016/j.renene.2022.06.141

Christophe, Y. (2019). Validation report of the CAMS near-real-time global atmospheric composition service: Period March–May 2019. *Copernicus Atmosphere Monitoring Service (CAMS) Report*, *February*.

Chu, Y., Li, M., & Coimbra, C. F. M. (2016). Sun-tracking imaging system for intra-hour DNI forecasts. *Renewable Energy*, *96*, 792–799. https://doi.org/10.1016/j.renene.2016.05.041

Chu, Y., Pedro, H. T. C., & Coimbra, C. F. M. (2013). Hybrid intra-hour DNI forecasts with sky image processing enhanced by stochastic learning. *Solar Energy*, *98*, 592–603. https://doi.org/https://doi.org/10.1016/j.solener.2013.10.020

Coimbra, C. F. M., Kleissl, J., Marquez, R., Mathiesen, P., Kleissl, J., Collier, C., Lave, M., Kleissl, J., Stein, J., Perez, R., Hoff, T. E. T. E., Stoffel, T., Urquhart, B., Ghonima, M., Nguyen, D. (Andu), Kurtz, B., Chow, C. W., Kleissl, J., Coimbra, C. F. M., … Larson, V. E. (2013). Chapter 15 - Stochastic-Learning Methods. In J. Kleissl (Ed.), *Solar Energy Forecasting and Resource Assessment* (pp. 21–48). Academic Press. https://doi.org/https://doi.org/10.1016/B978-0-12-397177-7.00015-2

Crawford, A., Price-Kelly, H., Terton, A., & Echeverría, D. (2016). Review of current and planned adaptation action in Burkina Faso. 55), 3(*4*, □□□□□ □□□□□. https://idl-bnc-

idrc.dspacedirect.org/handle/10625/55876

de Lima, F. J. L., dos Santos, T. S., da Silva Ramos, D. N., Weyll, A. L. C., Jacondino, W. D., Silva, A. R., Pereira, L. K. M., dos Santos, A. P. P., Melo Filho, J. B., de Carvalho Filho, M., Santos, A. Á. B., & Moreira, D. M. (2025). Evaluation of the short and medium-term forecast quality of global solar irradiance from GFS-MOS and WRF-Solar models for the northeast region of Brazil. *Energy Reports*, *13*, 2187–2203. https://doi.org/https://doi.org/10.1016/j.egyr.2025.01.073

Demir, V. (2025). Evaluation of Solar Radiation Prediction Models Using AI: A Performance Comparison in the High-Potential Region of Konya, Türkiye. *Atmosphere*, *16*(4). https://doi.org/10.3390/atmos16040398

DGESS. (2019). *Tableau De Bord 2018 Du Ministere De L'Energie*. 47.

Diagne, M., David, M., Boland, J., Schmutz, N., & Lauret, P. (2014). Post-processing of solar irradiance forecasts from WRF model at Reunion Island. *Solar Energy*, *105*, 99–108. https://doi.org/https://doi.org/10.1016/j.solener.2014.03.016

Díaz-Bedoya, D., González-Rodríguez, M. S., Clairand, J.-M., Serrano-Guerrero, X., & Escrivá-Escrivá, G. (2023). Forecasting Univariate Solar Irradiance using Machine learning models: A case study of two Andean Cities. *Energy Conversion and Management*, *296*, 117618.

Dommo, A., Vondou, D. A., Philippon, N., Eastman, R., Moron, V., & Aloysius, N. (2022). The ERA5's diurnal cycle of low-level clouds over Western Central Africa during June–September: Dynamic and thermodynamic processes. *Atmospheric Research*, *280*, 106426. https://doi.org/https://doi.org/10.1016/j.atmosres.2022.106426

Du, Y., Shi, H., Zhang, J., Xia, X., Yao, Z., Fu, D., Hu, B., & Huang, C. (2022). Evaluation of MERRA-2 hourly surface solar radiation across China. *Solar Energy*, *234*, 103–110. https://doi.org/https://doi.org/10.1016/j.solener.2022.01.066

Duffie, J. A., & Beckman, W. A. (2013). *Solar Engineering of Thermal Processes*. Solar Engineering of Thermal Processes. John Wiley & Sons.

Edwards, P. N. (2019). Predicting the Weather: An Information Commons for Europe and the World. *Cosmopolitan Commons*, *November*, 155–184. https://doi.org/10.7551/mitpress/8600.003.0009

Eissa, Y., Naseema Beegum, S., Gherboudj, I., Chaouch, N., Al Sudairi, J., Jones, R. K., Al Dobayan, N., & Ghedira, H. (2018). Prediction of the day-ahead clear-sky downwelling surface solar irradiances using the REST2 model and WRF-CHIMERE simulations over

the Arabian Peninsula. *Solar Energy*, *162*, 36–44. https://doi.org/https://doi.org/10.1016/j.solener.2018.01.003

Fraihat, H., Almbaideen, A. A., Al-Odienat, A., Al-Naami, B., De Fazio, R., & Visconti, P. (2022). Solar Radiation Forecasting by Pearson Correlation Using LSTM Neural Network and ANFIS Method: Application in the West-Central Jordan. *Future Internet*, *14*(3). https://doi.org/10.3390/fi14030079

Gallo, R., Castangia, M., Macii, A., Macii, E., Patti, E., & Aliberti, A. (2022). Solar radiation forecasting with deep learning techniques integrating geostationary satellite images. *Engineering Applications of Artificial Intelligence*, *116*, 105493. https://doi.org/https://doi.org/10.1016/j.engappai.2022.105493

Ginoux, P., Chin, M., Tegen, I., Prospero, J., Holben, B., Dubovik, O., & Lin, S.-J. (2001). Sources and distributions of dust aerosols simulated with the GOCART model. *Journal of Geophysical Research*, *106*, 20255–20274. https://doi.org/10.1029/2000JD000053

Haiden, T., Janousek, M., Vitart, F., Ben Bouallegue, Z., Ferranti, L., Prates, F., & Richardson, D. (2021). Evaluation of ECMWF forecasts, including the 2020 upgrade. *ECMWF Technical Memorandum*, *880*(December), 1–54.

Hayawi, K., Maliakkal, H., Venugopal, N., Hussain, T., & Rajagopalan, G. (2025). Machine Learning - Driven Solar Forecasting in Dust-Prone Regions for Sustainable Energy Systems. *Solar Energy Advances*, *5*, 100108. https://doi.org/10.1016/j.seja.2025.100108

Haywood, J. M., Pelon, J., Formenti, P., Bharmal, N., Brooks, M., & Capes, G. (2008). *Overview of the Dust and Biomass-burning Experiment and African Monsoon Multidisciplinary Analysis Special Observing Period-0 Overview of the Dust and Biomass-burning Experiment and African Monsoon Multidisciplinary Analysis Special Observing Period-0*. *December*. https://doi.org/10.1029/2008JD010077

Heimo, A. (2012). *COST Action ES1002 Weather Intelligence for Renewable Energies (WIRE) CURRENT STATE Report*. *August*, 1–164.

Hersbach, H., Bell, B., Berrisford, P., Hirahara, S., Horányi, A., Muñoz-Sabater, J., Nicolas, J., Peubey, C., Radu, R., Schepers, D., Simmons, A., Soci, C., Abdalla, S., Abellan, X., Balsamo, G., Bechtold, P., Biavati, G., Bidlot, J., Bonavita, M., … Thépaut, J. N. (2020). The ERA5 global reanalysis. *Quarterly Journal of the Royal Meteorological Society*, *146*(730), 1999–2049. https://doi.org/10.1002/qj.3803

Heubes, J., Schmidt, M., Stuch, B., García Márquez, J. R., Wittig, R., Zizka, G., Thiombiano, A., Sinsin, B., Schaldach, R., & Hahn, K. (2013). The projected impact of climate and land

use change on plant diversity: An example from West Africa. *Journal of Arid Environments*, *96*, 48–54. https://doi.org/https://doi.org/10.1016/j.jaridenv.2013.04.008

Hochreiter, S., & Schmidhuber, J. (1997). Long short-term memory. *Neural Computation*, *9*, 1735–1780. https://doi.org/https://doi.org/10.1162/neco.1997.9.8.1735

Huang, C. L., Wu, Y. K., Tsai, C. C., Hong, J. S., & Li, Y. Y. (2024). Revolutionizing Solar Power Forecasts by Correcting the Outputs of the WRF-SOLAR Model. *Energies*, *17*(1), 1–17. https://doi.org/10.3390/en17010088

Inman, R. H., Pedro, H. T. C., & Coimbra, C. F. M. (2013). Solar forecasting methods for renewable energy integration. *Progress in Energy and Combustion Science*, *39*(6), 535–576. https://doi.org/https://doi.org/10.1016/j.pecs.2013.06.002

Inness, A., Ades, M., Agustí-Panareda, A., Barr, J., Benedictow, A., Blechschmidt, A. M., Jose Dominguez, J., Engelen, R., Eskes, H., Flemming, J., Huijnen, V., Jones, L., Kipling, Z., Massart, S., Parrington, M., Peuch, V. H., Razinger, M., Remy, S., Schulz, M., & Suttie, M. (2019). The CAMS reanalysis of atmospheric composition. *Atmospheric Chemistry and Physics*, *19*(6), 3515–3556. https://doi.org/10.5194/acp-19-3515-2019

IPCC. (2013). *Climate Change 2013: The Physical Science Basis*.

Jiang, Y., Hua, D., Wang, Y., Yang, X., Di, H., & Yan, Q. (2024). *Attention-based CNN – LSTM deep learning hybrid model for the prediction of atmospheric ozone concentration*.

Jimenez, P. A., Hacker, J. P., Dudhia, J., Haupt, S. E., Ruiz-Arias, J. A., Gueymard, C. A., Thompson, G., Eidhammer, T., & Deng, A. (2016). WRF-SOLAR: Description and clear-sky assessment of an augmented NWP model for solar power prediction. *Bulletin of the American Meteorological Society*, *97*(7), 1249–1264. https://doi.org/10.1175/BAMS-D-14-00279.1

Jimenez, P., Hacker, J., Dudhia, J., Haupt, S., Ruiz-Arias, J., Gueymard, C., Thompson, G., Eidhammer, T., & Deng, A. (2016). WRF-Solar: Description and Clear-Sky Assessment of an Augmented NWP Model for Solar Power Prediction. *Bulletin of the American Meteorological Society*, *97*, 1249–1264. https://doi.org/10.1175/BAMS-D-14-00279.1

Kaiser, J. W., Heil, A., Andreae, M. O., Benedetti, A., Chubarova, N., Jones, L., Morcrette, J., & Razinger, M. (2012). *Biomass burning emissions estimated with a global fire assimilation system based on observed fire radiative power*. *x*, 527–554. https://doi.org/10.5194/bg-9-527-2012

Khamees, A. S., Sayad, T., Morsy, M., & Ali Rahoma, U. (2024). Evaluation of three radiation schemes of the WRF-Solar model for global surface solar radiation forecast: A case study

in Egypt. *Advances in Space Research*, *73*(6), 2880–2891. https://doi.org/https://doi.org/10.1016/j.asr.2023.12.010

Kirthiga, S. M., & Patel, N. R. (2018). Impact of updating land surface data on micrometeorological weather simulations from the WRF model. *Atmosfera*, *31*(2), 165–183. https://doi.org/10.20937/ATM.2018.31.02.05

Kottek, M., Grieser, J., Beck, C., Rudolf, B., & Rubel, F. (2006). World map of the Köppen-Geiger climate classification updated. *Meteorologische Zeitschrift*, *15*(3), 259–263. https://doi.org/10.1127/0941-2948/2006/0130

Kumi, N., Abiodun, B. J., Delano Thierry Odou, O., Heinrichs Ursula, H., Adamou, R., Lykke, A. M., Barfod, A. S., Tinggaard Svendsen, G., Greve, M., & Svenning, J. (2009). IOP Conference Series: Earth and Environmental Science Climate change mitigation by carbon stock-the case of semi-arid West Africa You may also like Potential impacts of 1.5 °C and 2 °C global warming on rainfall onset, cessation and length of rainy season in West Africa Climate change mitigation by carbon stock-the case of semi-arid West Africa. *IOP Conf. Ser.: Earth Environ. Sci*, *8*, 12004. https://doi.org/10.1088/1755-1315/8/1/012004

Kuye, A., & Jagtap, S. S. (1992). Analysis of solar radiation data for Port Harcourt, Nigeria. *Solar Energy*, *49*(2), 139–145. https://doi.org/https://doi.org/10.1016/0038-092X(92)90148-4

Lara-Fanego, V., Ruiz-Arias, J. A., Pozo-Vázquez, A. D., Gueymard, C. A., & Tovar-Pescador, J. (2012). Evaluation of DNI forecast based on the WRF mesoscale atmospheric model for CPV applications. *AIP Conference Proceedings*, *1477*, 317–322. https://doi.org/10.1063/1.4753895

Lara-Fanego, V., Ruiz-Arias, J. A., Pozo-Vázquez, D., Santos-Alamillos, F. J., & Tovar-Pescador, J. (2012a). Evaluation of the WRF model solar irradiance forecasts in Andalusia (southern Spain). *Solar Energy*, *86*(8), 2200–2217. https://doi.org/https://doi.org/10.1016/j.solener.2011.02.014

Lara-Fanego, V., Ruiz-Arias, J. A., Pozo-Vázquez, D., Santos-Alamillos, F. J., & Tovar-Pescador, J. (2012b). Evaluation of the WRF model solar irradiance forecasts in Andalusia (southern Spain). *Solar Energy*, *86*(8), 2200–2217. https://doi.org/10.1016/j.solener.2011.02.014

Li, H., Lian, Y., Wang, X., Ma, W., & Zhao, L. (2011). Solar constant values for estimating solar radiation. *Energy*, *36*(3), 1785–1789. https://doi.org/https://doi.org/10.1016/j.energy.2010.12.050

Li, M., Jin, H., & Shao, Q. (2021). Improvements in subseasonal forecasts of rainfall extremes by statistical postprocessing methods. *Weather and Climate Extremes*, *34*, 100384. https://doi.org/https://doi.org/10.1016/j.wace.2021.100384

Li, Q., Bessafi, M., & Li, P. (2023). Mapping Prediction of Surface Solar Radiation with Linear Regression Models: Case Study over Reunion Island. *Atmosphere*, *14*(9). https://doi.org/10.3390/atmos14091331

Linda A. Clark, D. P. (1992). Tree-Based Models. In T. J. H. (Eds. . J.M. Chambers (Ed.), *Routledge*. Wadsworth.

Liu, B. Y. H., & Jordan, R. C. (1960). The interrelationship and characteristic distribution of direct, diffuse and total solar radiation. *Solar Energy*, *4*(3), 1–19. https://doi.org/https://doi.org/10.1016/0038-092X(60)90062-1

Liu, Y., Qian, Y., Feng, S., Berg, L. K., Juliano, T. W., Jiménez, P. A., & Liu, Y. (2022). Sensitivity of solar irradiance to model parameters in cloud and aerosol treatments of WRF-solar. *Solar Energy*, *233*, 446–460. https://doi.org/https://doi.org/10.1016/j.solener.2022.01.061

Lorenz, E., Hurka, J., Heinemann, D., & Beyer, H. G. (2009). Irradiance Forecasting for the Power Prediction of Grid-Connected Photovoltaic Systems. *IEEE Journal of Selected Topics in Applied Earth Observations and Remote Sensing*, *2*(1), 2–10. https://doi.org/10.1109/JSTARS.2009.2020300

Luo, N., Zou, J., Zang, Z., Chen, T., & Yan, X. (2024). Wide and Deep Learning Model for Satellite-Based Real-Time Aerosol Retrievals in China. *Atmosphere*, *15*(5). https://doi.org/10.3390/atmos15050564

Ma, D., & Wang, W. (2023). *Evaluation of ERA5-Land reanalysis datasets for extreme temperatures in the Qilian Mountains of China*. *February*, 1–13. https://doi.org/10.3389/fevo.2023.1135895

Mabasa, B., Langerman, K., & Winkler, H. (2025). Evaluating the Global Horizontal Irradiance Projected by the Global Forecast System (GFS) Model in Diverse Climatic Zones in South Africa. *Weather and Forecasting*, *40*, 1047–1064. https://doi.org/10.1175/WAF-D-24-0074.1

Maka, A. O. M., & Alabid, J. M. (2022). Solar energy technology and its roles in sustainable development. *Clean Energy*, *6*(3), 476–483. https://doi.org/10.1093/ce/zkac023

Marquez, R., & Coimbra, C. F. M. (2013). Intra-hour DNI forecasting based on cloud tracking image analysis. *Solar Energy*, *91*, 327–336.

https://doi.org/https://doi.org/10.1016/j.solener.2012.09.018

Mendyl, A., Demir, V., Omar, N., Orhan, O., & Weidinger, T. (2024). Enhancing Solar Radiation Forecasting in Diverse Moroccan Climate Zones: A Comparative Study of Machine Learning Models with Sugeno Integral Aggregation. *Atmosphere*, *15*(1). https://doi.org/10.3390/atmos15010103

Murdan, A. P., & Armoogum, V. (2023). Comparing Machine Learning Techniques for Hourly Solar Power Generation Prediction. In J. Lu, H. Guo, I. McLoughlin, E. G. Chekole, U. Lakshmanan, W. Meng, P. C. Wang, & N. Heng Loong Wong (Eds.), *Proceedings of the 9th IRC Conference on Science, Engineering, and Technology* (pp. 365–376). Springer Nature Singapore.

Murphy, A. H. (1988). Skill Scores Based on the Mean Square Error and Their Relationships to the Correlation Coefficient. *Monthly Weather Review*, *116*(12), 2417–2424. https://doi.org/10.1175/1520-0493(1988)116<2417:SSBOTM>2.0.CO;2

Mwigereri, D. G., Ochieng, F. X., Ouma, J., Mwai, Z., & Mwalili, T. (2025). Evaluation of weather research forecasting-solar radiation schemes for solar power forecasting in equatorial Africa. *Energy Reports*, *13*, 4318–4330. https://doi.org/https://doi.org/10.1016/j.egyr.2025.04.004

Naveed, M. S., Iqbal, I., Hanif, M. F., Xiao, J., Liu, X., & Mi, J. (2025). Enhanced accuracy in solar irradiance forecasting through machine learning stack-based ensemble approach. *International Journal of Green Energy*, *0*(0), 1–24. https://doi.org/10.1080/15435075.2025.2450468

Nawab, F., Abd Hamid, A. S., Ibrahim, A., Sopian, K., Fazlizan, A., & Fauzan, M. F. (2023). Solar irradiation prediction using empirical and artificial intelligence methods: A comparative review. *Heliyon*, *9*(6), e17038. https://doi.org/10.1016/j.heliyon.2023.e17038

Odejobi, O. A., Alawode, K. O., & Lawal, M. O. (2024). EFFICIENT METHOD FOR FORECASTING SOLAR IRRADIANCE - A REVIEW. *FUDMA JOURNAL OF SCIENCES*, *8*(6 SE-Review Articles), 285–298. https://doi.org/10.33003/fjs-2024-0806-2786

Perez, R., David, M., Hoff, T. E., Jamaly, M., Kivalov, S., Kleissl, J., Lauret, P., & Perez, M. (2016). Spatial and Temporal Variability of Solar Energy. *Foundations and Trends® in Renewable Energy*, *1*(1), 1–44. https://doi.org/10.1561/2700000006

Perez, R., Lorenz, E., Pelland, S., Beauharnois, M., Van Knowe, G., Hemker, K., Heinemann, D., Remund, J., Müller, S. C., Traunmüller, W., Steinmauer, G., Pozo, D., Ruiz-Arias, J.

A., Lara-Fanego, V., Ramirez-Santigosa, L., Gaston-Romero, M., & Pomares, L. M. (2013). Comparison of numerical weather prediction solar irradiance forecasts in the US, Canada and Europe. *Solar Energy*, *94*, 305–326. https://doi.org/10.1016/j.solener.2013.05.005

Poudyal, K. N., Bhattarai, B. K., Sapkota, B., & Kjeldstad, B. (2012). Estimation of Global Solar Radiation Using Clearness Index and Cloud Transmittance Factor at Trans-Himalayan Region in Nepal. *Energy and Power Engineering*, *04*(06), 415–421. https://doi.org/10.4236/epe.2012.46055

Prasad, A. M., Iverson, L. R., & Liaw, A. (2006). Newer Classification and Regression Tree Techniques: Bagging and Random Forests for Ecological Prediction. *Ecosystems*, *9*(2), 181–199. https://doi.org/10.1007/s10021-005-0054-1

Prospero, J. M., Ginoux, P., Torres, O., Nicholson, S. E., & Gill, T. E. (2002). *ENVIRONMENTAL CHARACTERIZATION OF GLOBAL SOURCES OF ATMOSPHERIC SOIL DUST IDENTIFIED WITH THE NIMBUS 7 TOTAL OZONE MAPPING SPECTROMETER (TOMS) ABSORBING AEROSOL PRODUCT*. *February*, 1–31. https://doi.org/10.1029/2000RG000095

Sawadogo, W., Bliefernicht, J., Fersch, B., Salack, S., Guug, S., Diallo, B., Ogunjobi, K. O., Nakoulma, G., Tanu, M., Meilinger, S., & Kunstmann, H. (2023a). Hourly global horizontal irradiance over West Africa: A case study of one-year satellite- and reanalysis-derived estimates vs. in situ measurements. *Renewable Energy*, *216*, 119066. https://doi.org/https://doi.org/10.1016/j.renene.2023.119066

Sawadogo, W., Bliefernicht, J., Fersch, B., Salack, S., Guug, S., Diallo, B., Ogunjobi, K. O., Nakoulma, G., Tanu, M., Meilinger, S., & Kunstmann, H. (2023b). Hourly global horizontal irradiance over West Africa: A case study of one-year satellite- and reanalysis-derived estimates vs. in situ measurements. *Renewable Energy*, *216*. https://doi.org/10.1016/j.renene.2023.119066

Sawadogo, W., Fersch, B., Bliefernicht, J., Meilinger, S., Rummler, T., Salack, S., Guug, S., & Kunstmann, H. (2024). Evaluation of the WRF-solar model for 72-hour ahead forecasts of global horizontal irradiance in West Africa: A case study for Ghana. *Solar Energy*, *271*(March), 112413. https://doi.org/10.1016/j.solener.2024.112413

Sawadogo, W., Neya, T., Semde, I., Korahiré, J. A., Combasséré, A., Traoré, D. E., Ouedraogo, P., Diasso, U. J., Abiodun, B. J., Bliefernicht, J., & Kunstmann, H. (2024). Potential impacts of climate change on the sudan-sahel region in West Africa – Insights from

Burkina Faso. *Environmental Challenges*, *15*(February). https://doi.org/10.1016/j.envc.2024.100860

Saxena, N., Kumar, R., Rao, Y. K. S. S., Mondloe, D. S., Dhapekar, N. K., Sharma, A., & Yadav, A. S. (2024). Hybrid KNN-SVM machine learning approach for solar power forecasting. *Environmental Challenges*, *14*, 100838. https://doi.org/https://doi.org/10.1016/j.envc.2024.100838

Schmidt, M., Zizka, A., Traoré, S., Ataholo, M., Chatelain, C., Daget, P., Dressler, S., Hahn, K., Kirchmair, I., Krohmer, J., Mbayngone, E., Müller, J. V., Nacoulma, B., Ouédraogo, A., Ouédraogo, O., Sambaré, O., Schumann, K., Wieringa, J. J., Zizka, G., & Thiombiano, A. (2017). Diversity, distribution and preliminary conservation status of the flora of Burkina Faso. *Phytotaxa*, *304*(1), 1–215. https://doi.org/10.11646/phytotaxa.304.1.1

Si, Y., Wang, H., Wang, Y., Yang, H., Chen, Y., Liu, Q., Chen, S., & Zheng, N. (2021). Effects of single-layer low clouds on the surface solar radiation in East Asia. *Solar Energy*, *224*, 1099–1106. https://doi.org/https://doi.org/10.1016/j.solener.2021.06.047

Solano, E. S., Dehghanian, P., & Affonso, C. M. (2022). Solar Radiation Forecasting Using Machine Learning and Ensemble Feature Selection. *Energies*, *15*(19). https://doi.org/10.3390/en15197049

Soneye, O. O. (2021). Evaluation of clearness index and cloudiness index using measured global solar radiation data: A case study for a tropical climatic region of Nigeria. *Atmosfera*, *34*(1), 25–39. https://doi.org/10.20937/ATM.52796

Szymszová, S., Láska, K., Kim, S.-J., & Park, S.-J. (2025). Variability of solar radiation and cloud cover in the Antarctic Peninsula region. *Atmospheric Research*, *316*, 107940. https://doi.org/https://doi.org/10.1016/j.atmosres.2025.107940

Thaker, J., & Höller, R. (2023). Evaluation of High Resolution WRF Solar. *Energies*, *16*(8), 1–13. https://doi.org/10.3390/en16083518

Therneau, T. M., & Atkinson, E. J. (1997). *An introduction to recursive partitioning using the RPART routines. Mayo foundation, available from: http://www.mayo.edu/hsr/techrpt/61.pdf*. 52.

Tuccella, P., Menut, L., Briant, R., Deroubaix, A., Khvorostyanov, D., Mailler, S., Siour, G., & Turquety, S. (2019). Implementation of aerosol-cloud interaction within WRF-CHIMERE online coupled model: Evaluation and investigation of the indirect radiative effect from anthropogenic emission reduction on the Benelux Union. *Atmosphere*, *10*(1). https://doi.org/10.3390/atmos10010020

Verbyla, D. L. (1987). Classification trees: a new discrimination tool. *Canadian Journal of Forest Research*, *17*(9), 1150–1152. https://doi.org/10.1139/x87-177

Virgianto, R. H. (2024). *Assessing Solar Radiation Forecasting : a WRF-Solar Model Evaluation in Assessing Solar Radiation Forecasting : a WRF-Solar Model Evaluation in Kupang , Indonesia*. *May*. https://doi.org/10.56899/153.03.11

Voyant, C., Notton, G., Kalogirou, S., Nivet, M.-L., Paoli, C., Motte, F., & Fouilloy, A. (2017a). Machine learning methods for solar radiation forecasting: A review. *Renewable Energy*, *105*, 569–582. https://doi.org/https://doi.org/10.1016/j.renene.2016.12.095

Voyant, C., Notton, G., Kalogirou, S., Nivet, M. L., Paoli, C., Motte, F., & Fouilloy, A. (2017b). Machine learning methods for solar radiation forecasting: A review. *Renewable Energy*, *105*, 569–582. https://doi.org/10.1016/j.renene.2016.12.095

Wang, F., Yu, Y., Zhang, Z., Li, J., Zhen, Z., & Li, K. (2018). Wavelet decomposition and convolutional LSTM networks based improved deep learning model for solar irradiance forecasting. *Applied Sciences (Switzerland)*, *8*(8), 1–29. https://doi.org/10.3390/app8081286

Willmott, C. J. (1981). ON THE VALIDATION OF MODELS. *Physical Geography*, *2*(2), 184–194. https://doi.org/10.1080/02723646.1981.10642213

Winster Praveenraj, D. D., Madeswaran, A., Pastariya, R., Sharma, D., Abootharmahmoodshakir, K., & Dhablia, A. (2024). Machine Learning Integration for Enhanced Solar Power Generation Forecasting. *E3S Web of Conferences*, *540*, 0–6. https://doi.org/10.1051/e3sconf/202454004007

Yang, D. (2018). A correct validation of the National Solar Radiation Data Base (NSRDB). *Renewable and Sustainable Energy Reviews*, *97*, 152–155. https://doi.org/https://doi.org/10.1016/j.rser.2018.08.023

Yang, D., Alessandrini, S., Antonanzas, J., Antonanzas-Torres, F., Badescu, V., Beyer, H. G., Blaga, R., Boland, J., Bright, J. M., Coimbra, C. F. M., David, M., Frimane, Â., Gueymard, C. A., Hong, T., Kay, M. J., Killinger, S., Kleissl, J., Lauret, P., Lorenz, E., … Zhang, J. (2020). Verification of deterministic solar forecasts. *Solar Energy*, *210*, 20–37. https://doi.org/https://doi.org/10.1016/j.solener.2020.04.019

Yang, D., Kleissl, J., Gueymard, C. A., Pedro, H. T. C., & Coimbra, C. F. M. (2018). History and trends in solar irradiance and PV power forecasting: A preliminary assessment and review using text mining. *Solar Energy*, *168*, 60–101. https://doi.org/https://doi.org/10.1016/j.solener.2017.11.023

Yang, J., Kim, J.-H., Jiménez, P. A., Sengupta, M., Dudhia, J., Xie, Y., Golnas, A., & Giering, R. (2021). An efficient method to identify uncertainties of WRF-Solar variables in forecasting solar irradiance using a tangent linear sensitivity analysis. *Solar Energy*, *220*, 509–522. https://doi.org/https://doi.org/10.1016/j.solener.2021.03.044

Yang, J., Sengupta, M., Jiménez, P. A., Kim, J.-H., & Xie, Y. (2022). Evaluating WRF-Solar EPS cloud mask forecast using the NSRDB. *Solar Energy*, *243*, 348–360. https://doi.org/https://doi.org/10.1016/j.solener.2022.08.003

Yoon, J. W., Kim, H., Lee, S., & Park, S. K. (2025). *Comparative Evaluation of WRF and WRF-Solar for solar irradiance in South Korea*. *21*, 5194.

Younes, S., Claywell, R., & Muneer, T. (2005). Quality control of solar radiation data: Present status and proposed new approaches. *Energy*, *30*(9), 1533–1549. https://doi.org/https://doi.org/10.1016/j.energy.2004.04.031

Yu, P.-S., Yang, T.-C., Chen, S.-Y., Kuo, C.-M., & Tseng, H.-W. (2017). Comparison of random forests and support vector machine for real-time radar-derived rainfall forecasting. *Journal of Hydrology*, *552*, 92–104. https://doi.org/https://doi.org/10.1016/j.jhydrol.2017.06.020

Zamo, M., Mestre, O., Arbogast, P., & Pannekoucke, O. (2014). A benchmark of statistical regression methods for short-term forecasting of photovoltaic electricity production, part I: Deterministic forecast of hourly production. *Solar Energy*, *105*, 792–803. https://doi.org/https://doi.org/10.1016/j.solener.2013.12.006

Zhang, Y., Pan, Y., Wang, K., Fast, J. D., & Grell, G. A. (2010). WRF/Chem-MADRID: Incorporation of an aerosol module into WRF/Chem and its initial application to the TexAQS2000 episode. *Journal of Geophysical Research Atmospheres*, *115*(18). https://doi.org/10.1029/2009JD013443

Zhang, Y., Yan, Z., Zhu, H., & Tang, P. (2023). Physics-based model and data dual-driven approaches for predictive evacuation. *Developments in the Built Environment*, *16*, 100269. https://doi.org/https://doi.org/10.1016/j.dibe.2023.100269

Zhou, N., Shang, B., Xu, M., Peng, L., & Feng, G. (2024). Enhancing photovoltaic power prediction using a CNN-LSTM-attention hybrid model with Bayesian hyperparameter optimization. *Global Energy Interconnection*, *7*(5), 667–681. https://doi.org/10.1016/j.gloei.2024.10.005

Zhou, X., Liu, Y., Shan, Y., Endo, S., Xie, Y., & Sengupta, M. (2024). Influences of Cloud Microphysics on the Components of Solar Irradiance in the WRF-Solar Model.

Atmosphere, *15*(1). https://doi.org/10.3390/atmos15010039

Zwane, N., Tazvinga, H., Botai, C., Murambadoro, M., Botai, J., de Wit, J., Mabasa, B., Daniel, S., & Mabhaudhi, T. (2022). A Bibliometric Analysis of Solar Energy Forecasting Studies in Africa. *Energies*, *15*(15), 1–23. https://doi.org/10.3390/en15155520

Appendices

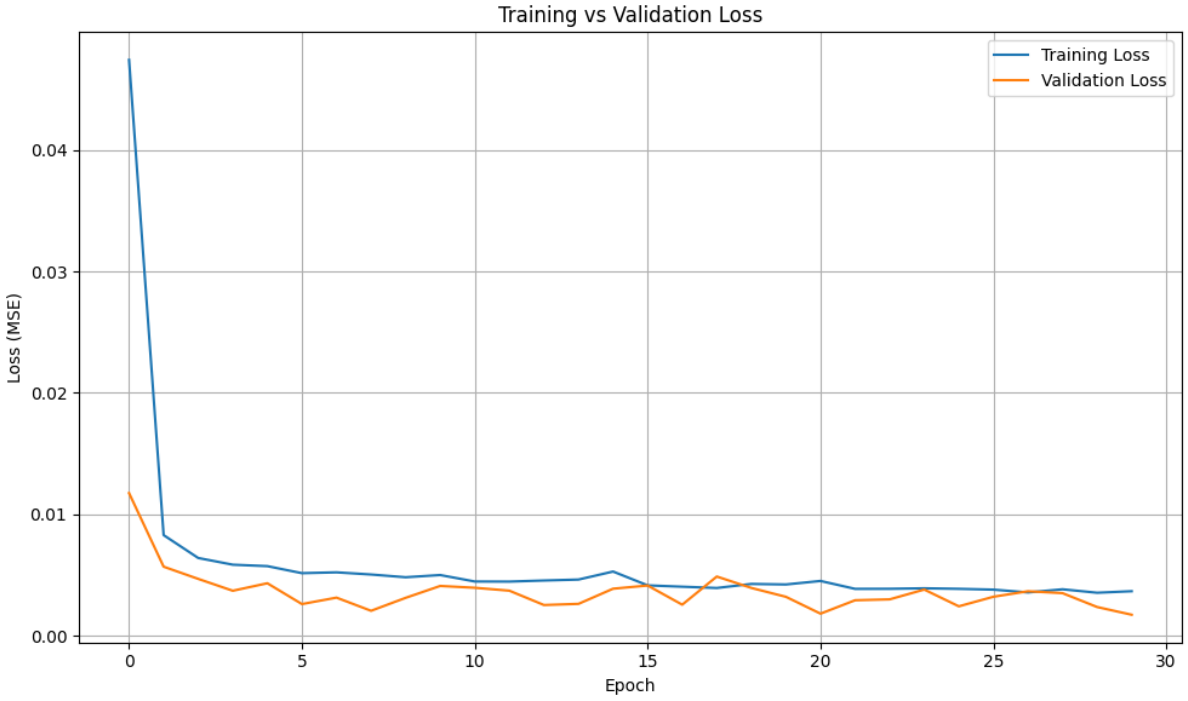

Figure 31: Loss function plot of LSTM.

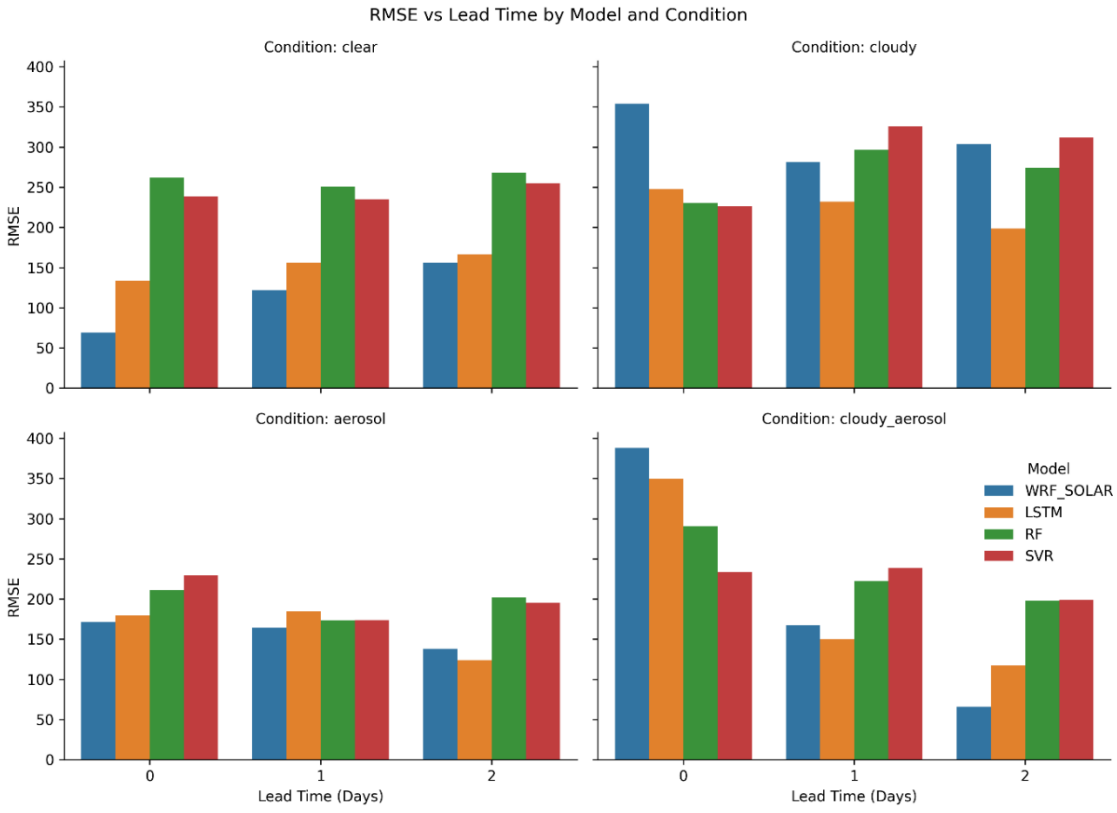

Figure 32: RMSE Comparison of different models.

Table of Contents